General Disclaimer

One or more of the Following Statements may affect this Document

- This document has been reproduced from the best copy furnished by the organizational source. It is being released in the interest of making available as much information as possible.

- This document may contain data, which exceeds the sheet parameters. It was furnished in this condition by the organizational source and is the best copy available.

- This document may contain tone-on-tone or color graphs, charts and/or pictures, which have been reproduced in black and white.

- This document is paginated as submitted by the original source.

- Portions of this document are not fully legible due to the historical nature of some of the material. However, it is the best reproduction available from the original submission.

NASA CR-165394

ORIENTATION DEPENDENCE OF THE STRESS RUPTURE PROPERTIES OF NICKEL-BASE SUPERALLOY SINGLE CRYSTALS

BY

REBECCA A. MACKAY AND RALPH D. MAIER
CASE WESTERN RESERVE UNIVERSITY

PREPARED FOR
NATIONAL AERONAUTICS AND SPACE ADMINISTRATION

MAY 1981

(NASA-CR-165394) ORIENTATION DEPENDENCE OF THE STRESS RUPTURE PROPERTIES OF NICKEL-BASE SUPERALLOY SINGLE CRYSTALS Contractor Report, Jun. 1979 - Jun. 1981 (Case Western Reserve Univ.) 37 p HC A03/MF A01 CSCL 20I G3/76

N83-13009

Unclas
00674

NASA LEWIS RESEARCH CENTER
GRANT NSG-3246

1. Report No. CR-165394	2. Government Accession No.	3. Recipient's Catalog No.
4. Title and Subtitle Orientation Dependence of the Stress Rupture Properties of Nickel-Base Superalloy Single Crystals		5. Report Date June 15, 1981 6. Performing Organization Code
7. Author(s) Rebecca A. MacKay		8. Performing Organization Report No. 10. Work Unit No.
9. Performing Organization Name and Address CaseWestern Reserve University Cleveland, Ohio 44106		11. Contract or Grant No. NSG-3246 13. Type of Report and Period Covered Contractor Report 6/79-6/81
12. Sponsoring Agency Name and Address National Aeronautics and Space Administration Washington, D. C. 20546		14. Sponsoring Agency Code

15. Supplementary Notes

16. Abstract The influence of orientation of the stress rupture behavior of Mar-M247 single crystals was studied. Stress rupture tests were performed at 724 MPa and 774°C where the effect of anisotropy is prominent.

The mechanical behavior of the single crystals was rationalized on the basis of the Schmid factors for the operative slip systems and the lattice rotations which the crystals underwent during deformation. The stress rupture lives were found to be greatly influenced by the lattice rotations required to produce intersecting slip, because steady-state creep does not begin until after the onset of intersecting slip. Crystals which required large rotations to become oriented for intersecting slip exhibited a large primary creep strain, a large effective stress level at the onset of steady-state creep, and consequently a short stress rupture life.

A unified analysis was attained for the stress rupture behavior of the Mar-M247 single crystals tested in this study at 774°C and that of the Mar-M200 single crystals tested in a prior study at 760°C. In this analysis, the standard [001]-[011]-[111] stereographic triangle was divided into several regions of crystallographic orientation which were rank ordered according to stress rupture life for this temperature regime. This plot indicates that those crystals having orientations within about 25° of the [001] exhibited significantly longer lives when their orientations were closer to the [001]-[011] boundary of the stereographic triangle than to the [001]-[$\bar{1}$11] boundary.

Therefore, the direction off the [001], as well as the number of degrees off the [001], has a major influence on the stress rupture lives of single crystals in this temperature regime. This finding has commercial significance because crystals with orientations near the [001] are utilized for most single crystal turbine blade applications. Hence, it may be appropriate to incorporate the effect of the direction off the [001] in pass/fail criteria employed to specify acceptable single crystal turbine blades.

17. Key Words (Suggested by Author(s))	18. Distribution Statement
Single crystals Nickel-base superalloy Stress rupture properties Mar-M247	Unclassified, unlimited

19. Security Classif. (of this report)	20. Security Classif. (of this page)	21. No. of Pages	22. Price*
Unclassified	Unclassified	95	

* For sale by the National Technical Information Service, Springfield, Virginia 22151

ORIENTATION DEPENDENCE OF THE STRESS RUPTURE PROPERTIES OF NICKEL-BASE SUPERALLOY SINGLE CRYSTALS

by

REBECCA ANN MACKAY

Submitted in partial fulfillment of the requirements

for the Degree of Master of Science

Department of Metallurgy and Materials Science

CASE WESTERN RESERVE UNIVERSITY

May 1981

ORIENTATION DEPENDENCE OF THE STRESS RUPTURE PROPERTIES OF NICKEL-BASE SUPERALLOY SINGLE CRYSTALS

Abstract

The influence of orientation on the stress rupture behavior of twenty-three Mar-M247 single crystals was studied. Stress rupture tests were performed at 724 MPa and 774^{o}C where the effect of anisotropy is prominent.

The mechanical behavior of the single crystals was rationalized on the basis of the Schmid factors for the operative slip systems and the lattice rotations which the crystals underwent during deformation. The stress rupture lives at 774^{o}C were found to be greatly influenced by the lattice rotations required to produce intersecting slip, because steady-state creep does not begin until after the onset of intersecting slip. Crystals which required large rotations to become ori-

ented for intersecting slip exhibited a large primary creep strain, a large effective stress level at the onset of steady-state creep, and consequently a short stress rupture life. Conversely, crystals which required little or no rotations to become oriented for intersecting slip exhibited much longer stress rupture lives.

Based on a consideration of the lattice rotations, the Schmid factors, and the stress rupture data, a unified analysis was attained for the stress rupture behavior of the Mar-M247 single crystals tested in this study at 774^{o}C and that of the Mar-M200 single crystals tested in a prior study at 760^{o}C. In this analysis, the standard [001] - [011] - [$\bar{1}$11] stereographic triangle was divided into several regions of crystallographic orientation which were rank ordered according to stress rupture life for this temperature regime. This plot indicates that the longest lives occurred for crystals having orientations near the [$\bar{1}$11]; long lives were exhibited by crystals having orientations near the [001]; and the shortest lives were exhibited by crystals oriented near the [011]. Those crystals having orientations within about 25° of the [001] exhibited significantly longer lives when their orientations were closer to the [001] - [011]

boundary of the stereographic triangle than to the [001] - [$\bar{1}$11] boundary.

Therefore, the direction off the [001], as well as the number of degrees off the [001], has a major influence on the stress rupture lives of single crystals in this temperature regime. This finding has commercial significance because crystals with orientations near the [001] are utilized for most single crystal turbine blade applications. Hence, it may be appropriate to incorporate the effect of the direction off the [001] in pass/fail criteria employed to specify acceptable single crystal turbine blades.

ACKNOWLEDGEMENTS

The author wishes to express her appreciation to:

Profs. R. D. Maier and L. J. Ebert for their guidance and support as thesis advisors;

The National Aeronautics and Space Administration for funding this work under NASA grant NSG-3246;

Dr. R. L. Dresnfield of the Lewis Research Center for providing the exothermically cast single crystals and technical assistance;

Mr. M. J. Woulds of Certified Alloy Products, Inc., for providing the Mar-M247 alloy;

Mr. J. Preston of TRW, Inc., for facilitating the production of the single crystals grown by the withdrawal process;

Dr. T. Kolakowski of TRW, Inc., and Mr. R. G. Garlick and Ms. M. I. Alley of the Lewis Research Center for useful discussions; and

Dr. H. R. Gray of the Lewis Research Center for his constant concern and support.

TABLE OF CONTENTS

LIST OF TABLES

LIST OF FIGURES

INTRODUCTION

Superalloy Development

The performance and efficiency of the aircraft gas turbine engine improve with increasing operating temperature. For this reason, considerable research has been directed toward developing turbine blade and vane materials capable of operating at increasingly higher temperatures in the high pressure section of the aircraft gas turbine engine. Over the past thirty years, nickel-base superalloys in particular have been found to possess the optimum combination of properties for this demanding application (1).

The widespread use of nickel-base alloys dates back to the 1940's when they were first introduced as heat-resistant materials in gas turbine engines (2). These alloys had a nickel-chromium base and possessed a combination of creep strength and oxidation resistance which surpassed that of the then available stainless steels. A major innovation occurred in superalloy development during World War II (3) when titanium and aluminum were added to the nickel-chromium solid solu-

tion strengthened superalloys to produce the precipitation hardenable superalloys. These additions produced the intermetallic compound known as γ', which is a $Ni_3(Al,Ti)$ ordered FCC phase. It is from these coherent precipitates that nickel-base superalloys obtain their superior strengths.

Significant improvements in the high temperature strength of superalloys were attained by compositional adjustments and new processing techniques. During the 1950's, vacuum melting was introduced (4) because it allowed the higher additions of aluminum and titanium to raise the γ' volume fraction, and because it permitted controlled additions of refractory elements for solid solution strengthening. Through the mid-1960's, continued alloy development further increased the γ' volume fraction by reducing the chromium content. However, the reduction in chromium content also decreased the oxidation resistance (5). Thus, it became apparent that an alternative approach was needed to attain higher usage temperatures for this family of alloys.

Directional Solidification

A major breakthrough in the investment casting process occurred with the introduction of unidirec-

tional solidification (6). This process provides a columnar grain structure in which the grain boundaries are oriented parallel to the major stress axis of the turbine blade. This columnar grain structure reduces the weakening influence of transverse grain boundaries and provides a creep resistance for directionally solidified (DS) superalloys which is superior to that for conventionally cast superalloys (6-9) with an equiaxed grain structure.

Columnar grain structures can be produced if heat is removed from the casting in one preferred direction during solidification. This preferential heat flow usually is achieved through the use of a water-cooled chill plate. This condition can be attained by pouring a superheated metal into the mold against the chill while concurrently establishing a suitable temperature gradient along the axial length of the mold with a furnace. Solidification starts at the chill in the form of an equiaxed structure, but the competitive growth between these randomly oriented equiaxed grains results in the development of a columnar structure with a preferred [001] orientation. It has been demonstrated (9-12) that the preferred [001] orientation of the columnar grains also contributes to the improvement in creep resistance of directionally solidified alloys.

The technology of unidirectional solidification has been developed to a high degree of sophistication. In the early Power-Down method (5,13-16), the solidification cycle was controlled by gradually reducing the power to the upper portion of an induction heater. A schematic diagram of this technique (13) is shown in Figure 1(a). Other techniques for heating the mold included electrical resistance heating (5) and the use of exothermic material (17).

High Rate Solidification, commonly known as the withdrawal process, was first introduced in 1971 (15), and is the predominant process used in the production of directionally solidified turbine airfoils (4,13, 14). In this process, the mold is mechanically withdrawn from the hot zone of the furnace, through a radiation baffle, and into a cooling chamber. Figure 1(b) is a schematic representation of this technique (13).

The Liquid Metal Cooling (LMC) technique has been developed more recently as another directional solidification process (18) and is illustrated in Figure 2 (13). In this process, the mold is lowered from the furnace hot zone, through a baffle, and into a cooling medium of rapidly circulating liquid tin. The LMC process makes it possible to grow dendritic structures

at substantially higher rates, thereby producing significantly finer microstructures. Finally, the exothermic DS process has been revived recently as a viable casting alternative which simultaneously offers significant reductions in turbine blade cost (19).

Single Crystal Production

The development of single crystal superalloys was the next logical step after the production of directionally solidified columnar grained material. It had been determined that the longitudinal grain boundaries in columnar grained structures contributed to their high temperature failure. Although these grain boundaries in general are parallel to the columnar growth direction, they are not linear but instead follow irregular paths between interlocking dendrite arms (9,10). These grain boundaries contain small sections transverse to tne major stress axis which are suitable locations for crack nucleation and growth. Thus, these transverse sections are similar to the transverse grain boundaries in conventionally cast material. Superalloy single crystals do not contain deleterious grain boundaries, and thus permit still higher operating temperatures to be attained in the aircraft gas turbine engine.

Single crysta'ɜ can be grown in the same equipment

and with essentially the same solidification techniques as the directionally solidified superalloys. The major difference is the placement of a multiple-turn constriction immediately above the initial growth zone, or "starter" block of the casting. The starter is used to establish columnar grain growth. As these grains grow through the multiple-turn constriction, one [001] grain survives the competitive growth process and continues to grow into the blade section of the mold.

This competitive growth process favors the [001] oriented grain because it is the direction of most rapid growth for cubic metals (20-22). The fact that the [001] orientation is naturally selected is fortuitous because this orientation provides the best combination of properties in the major stress axis of the turbine blade (10,23). This favorable orientation, and the lack of grain boundaries, are the major advantages of single crystal turbine blades. At all temperatures, [001] oriented single crystals exhibit both longer stress rupture lives and lower minimum creep rates than columnar grained material with a preferred [001] orientation (10,23).

Mechanical Properties of Single Crystals

Tensile Properties

The influence of orientation on the tensile behavior of Mar-M200 and Mar-M247 single crystals has been studied previously (10,24). The compositions of these and other selected nickel-base superalloys are presented in Table I. The tensile behavior was rationalized on the basis of Schmid's Law which is illustrated in Figure 3 (25) and states that:

$$\tau = (P/A) \cos \phi \cos \lambda,$$

where τ is the critical resolved shear stress (CRSS); (P/A) is the measured yield strength; ϕ is the angle between the normal to the slip plane and the tensile axis; λ is the angle between the slip direction and the tensile axis; and $\cos \phi \cos \lambda$ is the Schmid factor. The slip system with the highest Schmid factor is generally the first operative slip system because it is the system most favorably oriented for slip. Thus, the magnitude of the Schmid factor is an indicator of the ease with which a material undergoes slip.

The operative slip system for tensile testing up to 760°C has been found to be the $(111)[\bar{1}01]$ slip system (10,26,27). Deformation occurs by the shearing of the γ and γ' phases by $(a/2)\langle 110 \rangle$ superlattice pairs (26). The

Schmid factor contours for this slip system are presented in Figure 4, where they have been superimposed on the standard [001] - [011] - [$\bar{1}$11] stereographic triangle. The solid lines in the figure delineate orientations of constant Schmid factor of the values indicated. The Schmid factor contours presented in this study all have been produced by the present investigator according to a simple graphical technique (28) described in the literature.

The 0.02% yield strengths and percent elongations for the Mar-M247 single crystals tested between 23 and 760^{o}C are presented as a function of initial orientation in Figures 5(a) and (b), respectively (24). The data over this temperature range can be compared because the CRSS is virtually constant for the temperatures indicated, and thus the same slip system is operative. The Schmid factor contours from the [$\bar{1}$17] - [001] - [013] corner of the stereographic triangle in Figure 4 have been superimposed onto the tensile data in Figures 5(a) and (b). Comparison of these data with the Schmid factor contours demonstrates that single crystals with high Schmid factors are favorably oriented for slip and therefore generally exhibit lower strengths and higher ductilities. Crystals with low Schmid factors generally exhibit higher strengths and lower ductilities. Thus, the

tensile behavior of single crystals is related to the Schmid factor in a straightforward manner.

Creep and Stress Rupture Properties

The stress rupture behavior is somewhat more complex than the tensile benavior of nickel-base superalloys and is not fully understood. Initial studies (10) on the orientation and temperature dependence of the stress rupture properties of Mar-M200 revealed that, at 760°C, a substantial improvement in the stress rupture life occurs for crystals with orientations near the [001] and [$\bar{1}$11]. Conversely, very short lives were exhibited by specimens oriented near the [011]. At 871°C, high stress rupture lives also were obtained near the [001] and [$\bar{1}$11] orientations, however the influence of orientation is less pronounced than it is at 760°C. At 982°C, crystallographic orientation was found to have even less influence on the stress rupture life. The reduction in the influence of orientation with increasing temperature is a result of additional slip systems becoming operative at more elevated temperatures (10,29). The underlying mechanisms which describe the influence of orientation on the stress rupture life have not been fully elucidated. The orientation dependence of the stress rupture behavior cannot be explained by the Schmid factors alone.

Similar anisotropic behavior of the stress rupture properties was exhibited for exothermically cast Mar-M247 single crystals (24). The stress rupture lives are presented as a function of orientation in Figures 6(a) and (b) for the Mar-M247 single crystals tested under two different conditions: 774°C and 724 MPa; and 982°C and 207 MPa. These figures also demonstrate along with the Mar-M200 data that the effect of initial orientation is much more pronounced at lower testing temperatures.

Mechanistic studies (26,30,31) were undertaken to examine creep deformation at 760 and 857°C for Mar-M200 single crystals. At 760°C, primary creep was found to occur on the {111}<112> slip systems rather than on the {111}<110> slip systems. It was determined that (a/2)<112> dislocations are generated and then are dissociated into (a/6)<112> and (a/3)<112> partials. These (a/3)<112> partial dislocations then control primary creep by shearing the γ' precipitates by a diffusion-assisted process. Second-stage creep begins only after sufficient strain hardening occurs because of the interaction of {111}<112> slip systems. On the basis of activation energy studies (32), it was concluded that second-stage creep deformation occurs by slip on the {111}<110> slip systems and is controlled by the shearing of the γ' by (a/2)<110> dislocation pairs (31).

At 760°C (26), a short incubation period is required to generate the operative (a/2)<112> dislocations. The incubation period is followed by a rapid primary creep rate which is dependent on crystallographic orientation. The orientation dependence of both the rate and extent of primary creep was correlated with the Schmid factors and the multiplicity of slip for the {111}<112> systems. The primary creep strain and rate increased as a function of orientation in the following order: [001]; [001] - [011] boundary; region between the [001] - [011] and [001] - [$\bar{1}$11] boundaries; and [001] - [$\bar{1}$11] boundary. During primary creep, strain hardening was large for multiple slip orientations and small for single slip orientations.

For creep deformation at 857°C (31), it was found that pairs of (a/2)<110> dislocations shear the γ' in both primary and second-stage creep. The creep curves of these crystals did not include an incubation period, and the primary creep rate decreased continuously with time. The differences in steady-state creep rates were more striking as a function of orientation than were the primary creep strains. The orientation dependence of the steady-state creep rate at 857°C was explained by the nature of the dislocation junction reactions resulting from {111}<110> slip for different orientations. It was

determined that crystals along the [001] - [$\bar{1}$11] boundary had the lowest second-stage creep rates because of the formation of stable dislocation networks at the γ - γ' interfaces. The highest steady-state creep rates were exhibited by crystals oriented along the [001] - [011] boundary as a consequence of the low probability for the formation of stable junction reactions for crystals of these orientations. However, the overall effect of anisotropy among these specimens tested at 857^{o}C was less than the large orientation dependence of creep behavior at 760^{o}C.

The creep rupture behavior at 982^{o}C of the single crystal nickel-base superalloy designated as Alloy 444 (Table I) also has been examined (29). Unlike the Mar-M200 crystals at 857^{o}C, little difference was found among the specimens oriented near the [001] - [$\bar{1}$11] and the [001] - [011] boundaries of the stereographic triangle. Analysis of the lattice rotations of the failed specimens showed rotations of less than 4°. This indicates that slip is occurring on several slip systems at 982^{o}C. No incubation period was observed, and the extent of primary creep was very limited. The empirical results indicated that single crystals of this alloy could be misoriented as much as 26° off the [001] with no loss in creep strength at 982^{o}C.

Despite the advances made in identifying the mechanisms of creep deformation, the influence of orientation on stress rupture life is not fully understood. Furthermore, the stress rupture life data generated for nickel-base superalloy single crystals have been notably limited, particularly for orientations a few degrees off the [001] orientation. These orientations are currently being utilized in single crystal turbine blade applications. Typical criteria for acceptable single crystal turbine airfoils allow the orientations of the blade axes to range up to a designated maximum number of degrees from the [001] orientation. For example, a recently employed criterion specified 10° off the [001] as the maximum number of degrees off-axis allowed (33).

On the basis of the above discussion, it is clear that further investigation of the anisotropy of the stress rupture properties of nickel-base superalloy single crystals is warranted. The effects of anisotropy particularly for crystals with orientations near the [001] have important implications not only for the longitudinal properties, but for the transverse properties as well, because the root and lower portions of the turbine blade undergo significant stresses in directions transverse to the axis of the blade. It has been demonstrated (10,24) that the effect of crystallographic orientation

is much more pronounced at lower temperatures such as 760 and 774°C. This latter temperature is representative of the temperature above the root in the lower portion of the turbine blade in current and advanced aircraft engines (34).

Thus far, mechanistic studies (26,31) have indicated differences in creep rupture behavior among orientations along the [001] - [$\bar{1}$11] and [001] - [011] boundaries of the stereographic triangle near the commercially desirable [001] orientation. Dislocation interactions have been cited as reasons for such differences between boundary orientations at 857°C. However, the rotations that the crystals undergo during deformation which may actually lead to differences in dislocation interactions were not discussed. It is this more macroscopic cause which in particular requires additional consideration.

Statement of Purpose

The purpose of the present work was to attain an improved understanding of the orientation dependence of the stress rupture properties of Mar-M247 single crystals. This study evaluates the stress rupture properties generated for Mar-M247 single crystals and provides a unified analysis of these data as well as those reported for Mar-M200 (10,26). The improved fundamental understanding of the anisotropy provided by this study should assist in the successful implementation of single crystal airfoils.

MATERIAL AND EXPERIMENTAL PROCEDURE

Single Crystals

Eight single crystals* of Mar-M247 were grown by an adaptation of the exothermic process (33), and fifteen Mar-M247 single crystals** were produced by the withdrawal process. Chemical analyses were performed on several single crystals grown from both the exothermic and withdrawal processes. The compositions of the alloy are given in Table 1.

The 1.3 cm. diameter single crystal bars were solution treated in an argon atmosphere at 1232°C for two hours and then argon quenched. Subsequently, the crystals were aged at 816°C for 24 hours and air cooled to room temperature. Stress rupture specimens, with the configuration shown in Figure 7, were prepared by precision grinding.

---

* Produced by AiResearch Manufacturing Company of Arizona.

** Produced by TRW Metals - Turbine Components Division, Minerva, Ohio.

Mechanical Testing

Tensile tests were performed on single crystals produced by both the exothermic and withdrawal processes in order to fully characterize the material. These tests were performed at 23°C according to ASTM Specification E 8-69 (35). The crystals utilized had nearly identical orientations (within ±1°) and exhibited similar tensile properties.

Stress rupture tests were performed on the exothermically cast single crystals, as well as on four of the crystals produced by the withdrawal process, in a constant load creep frame according to ASTM Specification E 139-70 (36). Figure 7 shows the three Pt/Pt-10 Rd thermocouples which were attached at the top, middle, and bottom of the specimen gage section to ensure that the temperature along the gage length was maintained at 774 ± 2°C. The stress level utilized for these tests was 724 MPa.

Constant load creep rupture tests were performed at 774 ± 2°C and 724 MPa on eleven of the crystals which were grown by the withdrawal process. Extensometer knife edges were placed in ridges at the extremes of the specimen gage section, as shown in Figure 7. Creep extensions were measured automatically with the extensometers and were recorded continuously with linear variable differen-

tial transformers (LVDT's) and strip chart recorders until specimen failure. All creep measurements obtained were calculated directly from the strip charts upon which extension versus time were plotted for each creep rupture test. The following data were obtained: instantaneous strain on loading, ϵ_o; incubation time, t_i; primary creep rate, $\dot{\epsilon}_p$; primary creep strain, ϵ_p; strain at onset of second-stage creep, ϵ_s; and minimum creep rate, $\dot{\epsilon}_m$.

Laue Back-Reflection X-ray Technique

The initial orientations of each of the machined specimens, as well as the final orientations of selected crystals after stress rupture testing, were determined by the Laue back-reflection X-ray technique. A failed specimen half of each single crystal was chosen. The grip end of each specimen half was used to obtain the initial orientation of the crystal, whereas the gage section yielded the final orientation of each crystal after mechanical testing.

The grip end was rough ground on SiC papers of 240, 320, 400, and 600-grit size and then mechanically polished with 0.3 and 0.05 μm alumina on cloth-covered wheels. The fracture surface of each specimen half was sliced off on a slow speed diamond saw, and the cross

section of the gage length behind the fracture surface was mounted in epoxy. Rough grinding of this cross section was performed on 600-grit SiC paper, and the intermediate and final mechanical polishings were accomplished in the same manner as that for the grip end.

The polished surfaces were etched in a solution of 30% concentrated HCl and 70% H_2O_2 (30 vol. %) after each step of the polishing sequence in order to remove any cold-worked material produced during polishing. This procedure permitted a sharp diffraction pattern to be obtained. The polished specimen halves were placed in a fixture designed to align the specimen axis parallel to the X-ray beam. Laue patterns were taken from the grip ends of all the specimens and from the gage sections of selected specimens. The initial orientations of all the single crystals and the final orientations of selected specimens were determined.

Microscopy

The structures of the Mar-M247 single crystals produced by both the exothermic method and withdrawal process were examined and characterized by light and scanning electron microscopy. The specimens used for metallographic examination were removed from sections closest to the chill of the 1.3 cm. diameter single crystal bars.

The single crystals had received a complete heat treatment. The specimens were mounted in bakelite and were ground and polished in the same manner as that described for the grip end in the previous section.

Light microscopy was performed on both longitudinal sections and cross sections of near cube-oriented single crystals. The samples were examined first in the unetched condition to check for microporosity. Next, the samples were etched with a solution containing 30% concentrated HCl and 70% H_2O_2 (30 vol. %) to reveal both the microstructure and the macrostructure, the latter of which was revealed with a somewhat longer etching time.

Scanning electron microscopy was performed on cross sections of the single crystals to examine the size, shape, and distribution of the γ' precipitate both in the dendrite centers and in the interdendritic regions. Two etchants were utilized in order to reveal the desired features. An etch consisting of 33 parts H_2O, 33 parts CH_3COOH, 33 parts HNO_3, and 1 part HF was applied by immersion. This solution preferentially etched the γ' precipitate. A staining etch containing 4.5 grams NH_4FHF, 1.1 grams $K_2S_2O_5$, 100 ml. H_2O, and 50 ml. HCl was applied over the first etch by immersing the specimen in the solution for one minute. This second etchant colored the dendrites, making them easily visible

under the scanning electron microscope.

The γ' size was determined by measuring the sides of these precipitates on the scanning electron micrographs taken at magnifications of 10,000X. The γ' precipitates located in the dendrite cores, as well as the coarse cuboidal γ' located in the interdendritic interstices, were examined and measured in this size determination.

RESULTS AND DISCUSSION

Structure of the Single Crystals

Examination of the fully heat treated specimens by light and scanning electron microscopy revealed that the single crystals produced by the exothermic method and the withdrawal process were essentially the same in microstructure. Therefore in the discussion that follows, the crystals resulting from the two different solidification processes are not differentiated.

Although referred to as a "single crystal" material, Mar-M247 contains several phases. Its structure consists of ~60 volume percent of the coherent γ' precipitate in a matrix of γ, a nickel-rich solid solution. The γ' phase has an ordered FCC structure based on $Ni_3(Al,Ti)$ and is responsible for providing nickel-base superalloys with much of their superior strength. The interdendritic regions of Mar-M247 are interspersed additionally with MC carbides and small amounts of the $\gamma - \gamma'$ eutectic. Elemental segregation during solidification is responsible for the formation of the eutectic constituent and MC carbides (11,37). Heat treatment of

this material partially removes segregation, refines the γ' dispersion in the γ matrix, and eliminates some of the $\gamma - \gamma'$ eutectic. An example of the $\gamma - \gamma'$ eutectic contained in the interdendritic region of a fully heat treated Mar-M247 single crystal is shown in the lower left corner of Figure 8. The eutectic is composed of massive γ' particles which are separated by thin lamellae of γ. The γ' is shown to be preferentially etched in all of the scanning electron micrographs presented.

Solute segregation not only promotes the formation of the $\gamma - \gamma'$ eutectic and MC carbides but also affects the size of the γ' precipitate (37). Scanning electron microscopy shows clearly that the morphology of the γ' particles depends on the location within the dendritic structure. The micrograph in Figure 9(a) was taken at a magnification of 300X and shows the coring produced during solidification which remains after the material has been given a standard heat treatment. Figure 9(b) depicts the same area of the sample at 3000X and distinctly illustrates the change in γ' size at the interface between the dendrite core and interdendritic region.

The considerable differences in local solute composition (11) results in microstructural variations, because the solvus temperature is highest in the interdendritic regions where the solute content is higher

(14,38). Thus, precipitation of the γ' particles begins first and the γ' coarsens more in the interdendritic regions (39). Typical examples of the microstructure of a fully heat treated Mar-M247 single crystal in the dendrite core and in the interdendritic region are shown in Figures 10(a) and (b), respectively, at magnifications of 10,000X. The dendrite centers of all the single crystals examined have an average γ' particle size of about 0.28 μm, whereas the interdendritic regions contain large precipitates about 0.55 μm in size. The micrograph in Figure 10(b) shows that the interdendritic regions also contain fine γ' dispersed in between the relatively massive γ' after heat treatment. This fine γ' reprecipitates out when more aluminum and titanium are made available after the coarse γ' is partially redissolved during solution heat treatment (37).

In addition to the size difference, the shape of the γ' changes with respect to the location within the microstructure. The dendrite core shown in Figure 10(a) is composed of fairly regular cuboidal-shaped particles. However, Figure 10(b) shows that the large γ' precipitates in the interdendritic regions have a tendency to coalesce, appearing as groups of four in a polished surface. This ordered arrangement is actually a symmetrical cluster of eight cuboidal particles in three dimensions,

which has been described in detail as ogdoadically diced cubes that are cut by three mutually perpendicular planes (40). Figure 10(b) also shows that when the individual particles in the group become coarse, the extremities of the group become more irregular in shape.

Single crystals grown in the [001] orientation develop a unidirectional dendritic structure, because the [001] is the preferred direction of growth for dendrites in cubic metals. The typical macrostructure of a Mar-M247 single crystal grown in the cube direction is shown in Figures 11(a) and (b) for transverse and longitudinal sections, respectively. The primary dendrite arms are continuous in the [001] growth direction, as shown in the longitudinal section in Figure 11(b).

Mechanical Testing Data

Twenty-three Mar-M247 single crystals were stress rupture tested at 724 MPa and 774^{o}C where the effect of anisotropy is prominent. The results are summarized in Table II. Eight of these single crystals had been grown by an exothermic process which provided crystals with orientations that were scattered throughout the standard stereographic triangle. Fifteen additional single crystals were grown by the withdrawal process. Creep extensions were recorded continuously during the stress rup-

ture testing of eleven of these fifteen additional crystals. This latter testing further established the stress rupture behavior for orientations near the commercially desirable [001].

The wide variations in the stress rupture lives of the Mar-M247 single crystals tested at 774°C and 724 MPa are shown in Figure 12 as a function of orientation. Extremely low lives are exhibited near the [011], extremely high lives occur near the [$\bar{1}$11], and high lives are associated with the [001] orientation. However, there is also a region just a few degrees off the [001] where appreciably shorter lives occur. It is these wide differences in stress rupture lives particularly near the [001] that need further consideration.

Schmid Factors

Comparison of the stress rupture data with the appropriate Schmid factor contours did not reveal a simple relationship. The mechanisms involved are somewhat more complex than those for tensile testing. The {111}<112> slip system is operative during first-stage creep in the intermediate temperature range of 760°C (24,26,31). The Schmid factor contours for the most highly stressed {111}<112> slip systems are illustrated in Figure 13. The X - Y line in Figure 13 is the divid-

ing line between the two {111}<112> slip systems which have the highest values of Schmid factor for orientations within the stereographic triangle. This X - Y line is approximately 25° from the [001]. The $(\bar{1}11)[1\bar{1}2]$ slip system is operative for orientations within the triangle borders which lie to the left of the X - Y line; the $(111)[\bar{2}11]$ slip system is operative for orientations within the triangle borders which lie to the right of the X - Y line.

The crystal with the approximate $[\bar{1}11]$ orientation in Figure 12 exhibited the highest stress rupture life in part because the $[\bar{1}11]$ provides the lowest Schmid factor of 0.31 for first-stage creep. As shown in Figure 12, crystals with approximate [001] orientations had lives greater than 100 hours, whereas crystals with orientations near the [011] had lives of one hour or less. In this case, the Schmid factors do not explain the large differences in the stress rupture lives, because the [001] and [011] have equivalent Schmid factors of 0.47 for first-stage creep. Furthermore, the lives are appreciably shorter for crystals oriented a few degrees off the [001] compared with those of approximate [001] orientations, as shown in Figure 12. The [001] and the region of the triangle near the [001] have similar Schmid factors. Therefore, the Schmid factors cannot be utilized

to explain the differences in the stress rupture lives of these single crystals.

Lattice Rotations

During plastic deformation, single crystals rotate toward their slip direction, as is shown schematically for the gage section of the bar in Figure 14 (41). The directions of rotation within the stereographic triangle for the {111}<112> and (111)[$\bar{1}$01] slip systems are shown in Figures 15(a) and (b), respectively. For the {111}<112> slip system, the [001] - Y and X - [$\bar{1}$11] boundaries both represent regions of duplex slip in the standard stereographic triangle. Duplex slip regions are positions of crystallographic symmetry in which the Schmid factors are equivalent for two slip systems. This allows equal slip activity on two slip systems.

In the 760^{o}C temperature regime, single crystals oriented within the borders of the stereographic triangle initially deform during stress rupture testing by easy glide and rotate, as indicated by the arrows in Figure 15(a), under single slip until one of the duplex slip boundaries is reached, or nearly reached. The transition from first-stage to second-stage creep occurs only after sufficient intersecting slip between the {111}<112> slip systems strain hardens the material (26,42). During

second-stage creep, the (111)[$\bar{1}$01] slip system becomes operative (31), and the crystals rotate in the directions shown in Figure 15(b).

The lattice rotations determined by X-ray analysis for selected specimens stress rupture tested at 774^{o}C and 724 MPa are illustrated in Figure 16. The solid dots indicate the initial orientations of the crystals prior to testing, and the x's represent the orientations at the culmination of the test. The numbers associated with the rotations represent the stress rupture lives of the crystals in hours. Figure 16 shows two portions of the stereographic triangle which have been drawn on two different scales. The [001] corner in Figure 16(a) has been enlarged to show the detail of the rotations up to 10° from the [001] orientation.

The {111}<112> slip system appears to be operative for the single crystals when the lattice rotations in Figure 16 are compared to the rotations depicted in Figure 15(a). As illustrated in Figure 16(b), Specimens 2 and 158 were oriented initially near the [011] orientation and had lives of 0.5 hours and one hour, respectively. These crystals rotated through regions of high Schmid factor toward their slip direction during first-stage creep and failed before reaching the X - [$\bar{1}$11] boundary. The creep curve of Specimen 2 is illustrated

in Figure 17 and shows that the crystal actually failed during first-stage creep. Thus, no transition to steady-state creep occurred prior to failure. Specimen 147 is shown in Figure 16(b) as having life of 138 hours. Within experimental error, this crystal rotated to the X - [$\bar{1}$11] boundary prior to failure. In contrast, Crystal 157 in Figure 16(b) had an approximate [$\bar{1}$11] orientation and exhibited the longest stress rupture life of 1242 hours. This behavior is attributed to the multiple slip and to the minimum in Schmid factor that occur for a crystal having this orientation.

The rotations of the single crystals having orientations near the [001] are illustrated in Figure 16(a). Specimens 1 and B were oriented closest to the [001] and had stress rupture lives of 179 and 141 hours, respectively. Although both crystals were oriented initially for intersecting slip along the [001] - Y boundary, they were not located in a low Schmid factor region. Therefore, the two lives which resulted were significantly lower than that of the [$\bar{1}$11] crystal in Figure 16(b). The creep curve of Specimen B is illustrated in Figure 17 and shows regions of primary, steady-state, and tertiary creep. In contrast, Specimens ES and J were oriented approximately 10° off the [001] in the single slip region between the borders of the stereographic triangle in

Figure 16(a). These crystals were able to rotate to the [001] - Y boundary prior to the end of the creep rupture tests and exhibited lives of 53 and 26 hours, respectively. The creep curve of Specimen J in Figure 17 shows that the transition to steady-state creep was obtained prior to failure, although the slope of the second-stage creep regime was very high compared to that of Specimen B which had an approximate [001] orientation.

The creep rupture behavior of crystals oriented along the [001] - X boundary is similar to the behavior of crystals oriented within the borders of the stereographic triangle. Crystals initially oriented along this single slip [001] - X boundary deform by extensive easy glide and rotate toward the multiple slip [001] orientation. As illustrated in Figure 16(a), X-ray analysis showed that Specimen C rotated along the [001] - X boundary from 8° to 1° off the [001] during mechanical testing. This final orientation is further substantiated by the glide calculations presented in Appendix A, where it was also shown that this crystal could not have reached the multiple slip [001] orientation. As a result, the creep curve of Specimen C shows that a linear slope, characteristic of the steady-state creep regime, was not obtained. Thus, it appears that the transition into steady-state creep did not occur, and the specimen

exhibited a very short life of 14 hours. However, Specimens D, 33, and HS were oriented initially within 5.5° from the [001] along the [001] - X boundary. These crystals were able to rotate into intersecting slip regions of the stereographic triangle and had lives ranging from 59 to 80 hours. The creep curves of these crystals, in contrast to Crystal C, exhibited regions of primary, steady-state, and tertiary creep, as illustrated by the creep curve of Specimen HS in Figure 17.

Creep Rupture Data

To provide further insight into the influence of orientation, the creep rupture data which were generated for eleven of the twenty-three single crystals tested are discussed in some detail below. These data are summarized in Table III, and the following properties are included: instantaneous strain on loading, ϵ_o; incubation time, t_i; primary creep strain, ϵ_p; primary creep rate, $\dot{\epsilon}_p$; strain at the onset of second-stage creep, ϵ_s; and minimum creep rate, $\dot{\epsilon}_m$. The methods for measuring these creep data are described in Appendix B.

The primary creep strain, primary creep rate, strain at the onset of second-stage creep, and minimum creep rate are plotted as a function of orientation in

Figures 18(a)-(d) for the Mar-M247 single crystals creep rupture tested at 774°C and 724 MPa. The creep rates and strains of the crystals within 10.5° of the [001] increased with orientation in the following order: [001]; orientations along the [001] - [011] boundary; orientations between the [001] - [011] and [001] - [$\bar{1}$11] boundaries; and orientations along the [001] - [$\bar{1}$11] boundary. The [001] crystal was initially oriented for multiple slip, and the lowest values of ϵ_p and $\dot{\epsilon}_p$ were observed at this orientation. The [001] - [011] boundary represents duplex slip orientations, and intersecting slip occurs for crystals oriented along this boundary. Low values of ϵ_p, $\dot{\epsilon}_p$, ϵ_s, and $\dot{\epsilon}_m$ occurred for these orientations, and high lives resulted. In contrast, crystals oriented between the [001] - [$\bar{1}$11] and [001] - [011] boundaries and crystals oriented along the [001] - [$\bar{1}$11] boundary exhibited the highest creep strains and rates and the lowest creep rupture lives. These crystals deform by single slip until the duplex slip [001] - [011] boundary is reached.

An example of the importance of developing intersecting slip is demonstrated by comparing the creep data of Specimens C and ES in Table III and their corresponding rotations in Figure 16(a). Both crystals represent single slip orientations. However, Specimen C was ori-

ented 8° off the [001] along the [001] - [$\bar{1}$11] boundary, and Specimen ES was 10.5° off the [001] between the borders of the stereographic triangle. Although oriented farther away from the [001], Specimen ES actually was oriented closer to the [001] - [011] boundary. Crystal ES had lower creep rates and strains than Crystal C and exhibited a stress rupture life which was four times longer than that of Crystal C.

Mar-M200 Data

The anisotropic behavior of the Mar-M200 single crystals creep rupture tested at 760°C and 689 MPa (26) is in agreement with tnat of the Mar-M247 data generated in this study. The Mar-M200 data are presented as a function of orientation in Figures 19(a)-(c). In particular, Figure 19(a) shows rather strikingly for crystals 16 to 18° off the [001] that the primary creep strain substantially decreased from 12.5% along the single slip [001] - [$\bar{1}$11] boundary, to 6.3% between the triangle borders, and finally to 2.2% along the duplex slip [001] - [011] boundary.

Further substantiation of the stress rupture behavior was provided by the Mar-M200 single crystals tested at 760°C and 689 MPa (10). Tne stress rupture lives are shown as a function of orientation in Figure 20

(10). There were two crystals of particular interest, both of which were oriented approximately 12° off the [001]. The crystal which was oriented closer to the duplex slip [001] - [011] boundary had a life of 466 hours, whereas the crystal which was oriented closer to the single slip [001] - [$\bar{1}$11] boundary had a life of only 12 hours. Thus, an order of magnitude difference exists between the lives of two crystals, both oriented the same number of degrees from the [001], but oriented in different directions from the [001]. Furthermore, it appears from these experimental data plotted in Figure 20 that crystals may be oriented farther off-axis along the [001] - [011] boundary than crystals with equivalent stress rupture lives along the [001] - [$\bar{1}$11] boundary.

Although the actual lattice rotations were not determined in the Mar-M200 study (10), single slip was confirmed by the present investigator for the 12-hour life specimen by computing the elongation necessary to reach the duplex slip [001] - [011] boundary. The details of this computation are presented in Appendix A. The measured elongation after failure listed for this 12-hour life specimen was 10.3% (10); however, the elongation necessary to obtain duplex slip regions of the triangle was computed in Appendix A to be 25.4%. Clearly, this specimen never reached the duplex slip [001] -

[011] boundary, and an extremely short stress rupture life resulted for this crystal.

Factors Influencing Rupture Lives

Based on the stress rupture lives, creep rupture data, and lattice rotations for Mar-M247 and the empirical data reported for Mar-M200 (10,26), it was determined that the primary factor which influenced the stress rupture lives of the single crystals was the amount of lattice rotation required to produce intersecting slip. The lattice rotations influence the lives by directly affecting the amount of strain that the crystal undergoes during primary creep. During first-stage creep, the single crystal deforms by easy glide, and the material can elongate appreciably for single slip orientations, as exemplified by Specimen C in Figure 17. The transition from first-stage to second-stage creep begins only after intersecting slip sufficiently strain hardens the material. Therefore, second-stage creep cannot begin until the crystal has rotated to, or nearly to, the [001] - Y or the X - $[\bar{1}11]$ duplex slip boundary.

On the basis of the analysis described above, it was hypothesized that the smaller the rotation required to initiate intersecting slip, the sooner second-stage creep will begin, and the longer the stress rupture life

will be. Smaller amounts of first-stage creep provide a smaller reduction in the load-bearing cross section of the specimen prior to the onset of steady-state creep. Thus, the effective stress level at the beginning of steady-state creep should be lower, and the stress rupture life should be longer, for smaller amounts of primary creep.

The effective stress level at the onset of second-stage creep for the Mar-M247 single crystals creep rupture tested at 774°C and a nominal stress of 724 MPa was found to be influenced greatly by crystallographic orientation. The details of this computation are given in Appendix C. The effective stress level at the onset of steady-state creep ranged from 753 MPa for Specimen B, which had an approximate [001] orientation, to 790 MPa for Specimen C, which was oriented 8° off the [001] along the single slip [001] - X boundary. Specimen B had an $\dot{\varepsilon}_m$ equal to 2.03×10^{-4} hr.$^{-1}$ and a 141 hour life; Specimen C had an $\dot{\varepsilon}_m$ equal to 15.2×10^{-4} hr.$^{-1}$ and a 14 hour life. Thus, a higher effective stress level at the onset of second-stage creep corresponded to a higher steady-state creep rate. Since the rupture lives of most metals are inversely proportional to the steady-state creep rates (31), any increase in this creep rate will shorten the life of the crystal. Thus, the rupture lives

will be longer for smaller amounts of rotations to intersecting slip regions, because the effective stress levels will be lower for smaller amounts of primary creep.

In view of the above, the empirical observations of the stress rupture behavior of the Mar-M247 single crystals can be explained by the lattice rotations which the crystals underwent during mechanical testing at 774°C. Specimens oriented along directions of high symmetry, such as the approximate [$\bar{1}$11] and [001] orientations of Specimens 157 and B, respectively, exhibited the longest stress rupture lives because they were initially oriented for intersecting slip. Crystals which required large rotations to become oriented for intersecting slip, such as Specimens C, 2, and 158, had the shortest lives because they did not benefit from the strengthening effects of intersecting slip and second-stage creep was not obtained. Crystals oriented such that small elongations caused them to rotate into intersecting slip orientations exhibited intermediate lives.

Potential Commercial Applications

Based on a consideration of the lattice rotations, the creep and stress rupture data, and the Schmid factors for the Mar-M247 single crystals stress ruptured tested at 774°C, the standard [001] - [011] - [$\bar{1}$11] stereographic

triangle was divided into several regions which were rank ordered according to stress rupture life for this temperature regime. This plot shown in Figure 21 indicates that the longest lives were exhibited by crystals having orientations near the [$\bar{1}$11]; long lives were exhibited by crystals having orientations near the [001]; and the shortest lives were exhibited by crystals near the [011]. The single crystal data generated in the present study agree reasonably well with the plot. Comparison of the creep rupture data for the Mar-M200 single crystals (10,26) shown in Figures 19-20 with this plot provides further verification of its validity.

Those crystals having orientations within about 25° of the [001] exhibited significantly longer lives when their orientations were closer to the [001] - [011] boundary of the stereographic triangle than to the [001] - [$\bar{1}$11] boundary. It was determined that crystals oriented closer to the [001] - [011] boundary do not have to rotate as far before reaching intersecting slip regions during first-stage creep. Accordingly, the plot in Figure 21 predicts low lives in the region of the triangle greater than 7° off the [001] in the [001] - [$\bar{1}$11] direction. This latter finding in particular has commercial significance. Although the [$\bar{1}$11] orientation may be the most creep-resistant in this temperature regime,

crystals with orientations near the [001] are utilized for most single crystal turbine applications, because the [001] provides high stress rupture lives and excellent thermal fatigue resistance as a result of its low elastic modulus (10).

Typical criteria for acceptable single crystal turbine airfoils allow the orientations of the blade axes to range up to a designated maximum number of degrees from the [001] orientation. For example, a recently employed criterion specified 10° off the [001] as the maximum number of degrees off-axis allowed (33). According to Figure 21, this particular pass-fail standard encompasses regimes of the stereographic triangle which provide both very good and poor stress rupture lives. Furthermore, a criterion of this type would accept a crystal which exhibited a 12-hour life under the testing conditions utilized for the Mar-M200 crystals in Figure 20 (10) and would reject another crystal, tested under the same conditions, with an orientation which provided a 725-hour life.

It was determined in this study that the direction off the [001], as well as the number of degrees off the [001], has a major influence on the stress rupture lives of single crystals in this temperature regime. Therefore, it may be appropriate to incorporate the effect of

the direction off the [001] when establishing pass-fail criteria for acceptable single crystal turbine blades. Thus, the plot of suggested regimes of stress rupture lives for Mar-M247 and Mar-M200 single crystals in Figure 21 should assist in establishing standards for commercially acceptable orientations of single crystal turbine airfoils.

CONCLUSIONS

1. For stress rupture testing at 774°C, crystals which required large rotations to become oriented for intersecting slip had the shortest lives; those which required little or no rotations had the longest lives.

2. The amount of lattice rotation required for a crystal to become oriented for intersecting slip directly influences the amount of strain that the crystal undergoes during primary creep, because steady-state creep does not begin until after the onset of intersecting slip. The smaller the primary creep strain is, the smaller the reduction in load-bearing cross section will be, and the lower the effective stress level will be at the onset of steady-state creep.

3. Although crystals near the [001] and [$\bar{1}$11] were both favorably oriented for intersecting slip at 774°C, the [$\bar{1}$11] orientation provided much longer stress rupture lives because of lower Schmid factors.

4. Crystals having orientations within about 25° of the [001] exhibited longer lives when oriented closer

to the [001] - [011] boundary of the stereographic triangle than to the [001] - [$\bar{1}$11] boundary during stress rupture testing at 760 and 774^{o}C.

5. It may be appropriate to incorporate the effect of direction off the [001], as well as the number of degrees off the [001], when establishing pass-fail criteria for acceptable single crystal turbine blades.

REFERENCES

(1) D. N. Duhl and E. R. Thompson: "Directional Structures for Advanced Aircraft Turbine Blades," J. Aircraft, June 1977, vol. 14, pp. 521-526.

(2) W. F. Simmons: "Current and Future Materials Usage in Aircraft Gas Turbine Engines," MCIC 73-14, p. 1, Battelle Memorial Institute, June 1973.

(3) W. A. Owczarski: "Process and Metallurgical Factors in Joining Superalloys and Other High Service Temperature Materials," in Advanced Manufacturing Techniques in Joining of Aerospace Materials, p. 3-3, AGARD, Sept. 1977.

(4) F. L. VerSnyder and E. R. Thompson: "Superalloys for Gas Turbines - Another 20 Years ," Climax Molybdenum Co. Conference for Alloys For the 80's, Ann Arbor, Mich., June 17-18, 1980, in press.

(5) F. L. VerSnyder and M. F. Shank: "The Development of Columnar Grain and Single Crystal High Temperature Materials Through Directional Solidification," Mater. Sci. Eng., 1970, vol. 6, pp. 213-247.

(6) F. L. VerSnyder and R. W. Guard: "Directional Grain Structures for High Temperature Strengtn," Trans. ASM, 1960, vol. 52, pp. 485-493.

(7) B. J. Piearcey and F. L. VerSnyder: "New Casting Technique Strengthens Turbine Components," SAE J., June 1966, vol. 74, no. 6, pp. 84-87.

(8) F. L. VerSnyder, R. B. Barrow, L. W. Sink, and B. J. Piearcey: "Directional Solidification in the Precision Casting of Gas-Turbine Parts," Modern Cast., Sept. 1967, vol. 52, no. 6, pp. 68-75.

(9) B. J. Piearcey and B. E. Terkelsen: "The Effect of Unidirectional Solidification on the Properties of Cast Nickel-Base Superalloys," Trans. TMS-AIME, Aug. 1967, vol. 239, pp. 1143-1150.

(10) B. H. Kear and B. J. Piearcey: "Tensile and Creep Properties of Single Crystals of the Nickel-Base Superalloy Mar-M200," Trans. TMS-AIME, Aug. 1967, vol. 239, pp. 1209-1215.

(11) B. J. Piearcey, B. H. Kear, and R. W. Smashey: "Correlation of Structure with Properties in a Directionally Solidified Nickel-Base Superalloy," Trans. ASM, 1967, vol. 60, pp. 634-645.

(12) B. H. Kear and A. F. Giamei: "Manipulation of Superalloy Microstructures and Properties By Advanced Processing Techniques," in Fundamental Aspects of Structural Alloy Design, R. I. Jaffe and B. A. Wilcox, eds., pp. 461-485, Plenum Publishing Corporation, New York, 1977.

(13) C. P. Sullivan, A. F. Giamei, and F. L. VerSnyder: "Some Aspects of Directional Solidification in the Production of Superalloy Ingots," Fifth Int'l. Symp. on Electroslag and Other Special Melting Technologies - Part III, G. H. Bhat and A. Simkovich, eds., pp. 525-594, Carnegie-Mellon Institute of Research, Pittsburgh, 1975.

(14) A. F. Giamei, E. H. Kraft, and F. D. Lemkey: "The Art and Science of Unidirectional Solidification," in New Trends in Materials Processing, C. S. Hartley, ed., pp. 48-97, American Soc. for Metals, Metals Park, Ohio, 1976.

(15) A. F. Giamei and J. S. Erickson: "Computer Applications in Directional Solidification Processing," Third Int'l. Symp. on Superalloys, Seven Springs, PA, Sept. 1976, B. H. Kear, et. al., eds., pp. 405-424, Claitor's Publishing Division, Baton Rouge, 1976.

(16) J. E. Northwood: "Improving Turbine Blade Performance by Solidification Control," Metallurgia, July 1979, pp. 437-442.

(17) M. C. Flemings, R. V. Barone, S. Z. Uram, and H. F. Taylor: "Solidification of Steel Castings and Ingots," Trans. Am. Foundrymen's Soc., 1961, vol. 69, pp. 422-435.

(18) A. F. Giamei and J. G. Tschinkel: "Liquid Metal Cooling: A New Solidification Technique," Met. Trans., Sept. 1976, vol. 7, pp. 1427-1434.

(19) G. S. Hoppin, III, M. Fujii, and L. W. Sink: "Development of Low-Cost Directionally Solidified Turbine Blades," Fourth Int'l. Symp. on Superalloys, Seven Springs, PA, Sept. 1980, J. K. Tien, et. al., eds., pp. 225-234, American Society for Metals, Metals Park, Ohio, 1980.

(20) B. Chalmers: in Principles of Solidification, p. 117, John Wiley & Sons, Inc., New York, 1964.

(21) M. C. Flemings: in Solidification Processing, p. 73, McGraw-Hill Book Company, New York, 1974.

(22) G. A. Chadwick: "A Hard-Sphere Model of Crystal Growth," Metal Sci. J., Sept. 1967, vol. 1, pp. 132-139.

(23) F. L. VerSnyder and B. J. Piearcey: "Single Crystal Alloy Extends Turbine Blade Service Four Times," SAE J., Aug. 1966, vol. 74, no. 8, pp. 36-42.

(24) R. A. MacKay, R. L. Dreshfield, and R. D. Maier: "Anisotropy of Nickel-Base Superalloy Single Crystals," Fourth Int'l. Symp. on Superalloys, Seven Springs, PA, Sept. 1980, J. K. Tien, et. al., eds., pp. 385-394, American Society for Metals, Metals Park, Ohio, 1980.

(25) G. E. Dieter: in Mechanical Metallurgy, 2nd ed., p. 128, McGraw-Hill Book Company, New York, 1976.

(26) G. R. Leverant and B. H. Kear: "The Mechanism of Creep in Gamma Prime Precipitation-Hardened Nickel-Base Alloys at Intermediate Temperatures," Met. Trans., Feb. 1970, vol. 1, pp. 491-498.

(27) S. M. Copley and B. H. Kear: "Temperature and Orientation Dependence of the Flow Stress in Off-Stoichiometric Ni_3Al (γ' Phase)," Trans. TMS-AIME, July 1967, vol. 239, pp. 977-984.

(28) C. S. Hartley and J. P. Hirth: "Resolution of Stresses in Single-Crystal Deformation," Trans. TMS-AIME, July 1965, vol. 233, pp. 1415-1419.

(29) D. N. Duhl, M. Gell, A. F. Giamei, and G. R. Leverant: "Deformation and Fracture of Advanced Anisotropic Superalloys," AFOSR Contract No. F44620-76-C-0028, Interim Technical Report, Nov. 1977.

(30) B. H. Kear, G. R. Leverant, and J. M. Oblak: "An Analysis of Creep-Induced Intrinsic/Extrinsic Fault Pairs in a Precipitation Hardened Nickel-Base Alloy," Trans. Quart. ASM, 1969, vol. 62, pp. 639-650.

(31) G. R. Leverant, B. H. Kear, and J. M. Oblak: "Creep of Precipitation-Hardened Nickel-Base Alloy Single Crystals at High Temperatures," Met. Trans., Jan. 1973, vol. 4, pp. 355-362.

(32) J. K. Tien, B. H. Kear, and G. R. Leverant: "On the High Activation Energy for Steady State Creep of Particle Strengthened Systems," Scripta Met., Feb. 1972, vol. 6, pp. 135-139.

(33) T. E. Strangman, G. S. Hoppin III, C. M. Phipps, K. Harris, and R. E. Schwer: "Development of Exothermically Cast Single-Crystal Mar-M247 and Derivative Alloys," Fourth Int'l. Symp. on Superalloys, Seven Springs, PA, Sept. 1980, J. K. Tien, et. al., eds., pp. 215-224, American Society for Metals, Metals Park, Ohio, 1980.

(34) D. N. Duhl: Personal Communication, Sept. 1980.

(35) E 8-69: "Standard Methods of Tension Testing of Metallic Materials," in 1974 Annual Book of ASTM Standards, Part 10, pp. 90-110, American Society for Testing and Materials, Philadelphia, 1974.

(36) E 139-70: "Standard Recommended Practice for Conducting Creep, Creep-Rupture, and Stress-Rupture Tests of Metallic Materials," in 1974 Annual Book of ASTM Standards, Part 10, pp. 229-245, American Society for Testing and Materials, Philadelphia, 1974.

(37) J. J. Jackson, M. J. Donachie, R. J. Henricks, and M. Gell: "The Effect of Volume Percent of Fine γ' on Creep in DS Mar-M200 + Hf," Met. Trans., Oct. 1977, vol. 8, pp. 1615-1620.

(38) T. Z. Kattamis and J. C. Lecomte: "A Novel Method for the Establishment of Solvus Surfaces as Demonstrated with Nickel-Base Alloys," J. Mater. Sci., Dec. 1978, vol. 13, pp. 2731-2736.

(39) G. D. Merz, T. Z. Kattamis, and A. F. Giamei: "Microsegregation and Homogenization of Ni - 7.5 wt% Al - 2.0 wt% Ta Dendritic Monocrystals," J. Mater. Sci., Mar. 1979, vol. 14, pp. 663-670.

(40) J. H. Westbrook: "Precipitation of Ni_3Al from Nickel Solid Solution as Ogdoadically Diced Cubes," Zeits fur Krist, 1958, vol. 110, p. 1.

(41) R. H. Hertzberg: in Deformation and Fracture Mechanics of Engineering Materials, p. 85, John Wiley & Sons, New York, 1976.

(42) G. R. Leverant and D. N. Duhl: "The Effect of Stress and Temperature on the Extent of Primary Creep in Directionally Solidified Nickel-Base Superalloys," Met. Trans., March 1971, vol. 2, pp. 907-908.

(43) E. Schmid and W. Boas: in Plasticity of Crystals, pp. 57-58, F. A. Hughes & Co. Limited, London, 1950.

(44) D. K. Bowen and J. W. Christian: "The Calculation of Shear Stress and Shear Strain for Double Glide in Tension and Compression," Philos. Mag., Aug. 1965, vol. 12, 8th series, no. 116, pp. 369-378.

TABLES

TABLE 1

COMPOSITIONS OF SELECTED NICKEL-BASE SUPERALLOYS (wt. %)

ELEMENTS	ALLOYS				
	Mar-M200[a]	Mar-M200[b]	Alloy 444[c]	Mar-M247[d]	Mar-M247[e]
C	0.15	~50ppm	-	0.13	0.14
Cr	9.0	8.95	8.6	8.3	7.9
Co	10.0	10.55	-	9.9	9.5
Ti	2.0	1.65	1.98	0.93	0.96
Al	5.0	4.65	5.1	5.6	5.8
W	12.5	11.85	11.1	10.2	9.6
Zr	0.05	0.041	-	0.06	0.03
B	0.015	0.011	-	0.018	0.013
Fe	1.5 max	-	-	0.10 max	0.10 max
Nb	-	0.61	0.91	0.05 max	0.05 max
Mo	-	-	-	0.72	0.76
Ta	-	-	-	2.96	3.06
Hf	-	-	-	1.23	1.50
Ni	bal.	bal.	bal.	bal.	bal.

a Utilized in Ref. 10.

b Utilized in Refs. 26, 30, 31. Weight percent listed is an average of the compositional range.

c Utilized in Ref. 29.

d Utilized in Ref. 24 and in the present study (exothermic process).

e Utilized in the present study (withdrawal process).

TABLE II

STRESS RUPTURE DATA OF MAR-M247 SINGLE CRYSTALS

TESTED AT 774°C and 724 MPa

SPECIMEN	LIFE, hr	ELONG., percent	R.A., percent	ORIENTATION, DEGREES FROM: [001]	[011]
1	179	16	15	3	42
72	26	9	12	7	38.5
74	21	11	13	10	36
123	37	12	15	8	37.5
128	20	8	12	28	17
147	138	8	15	45	28
157	1242	11	12	52.5	34.5
158	1	24	28	39	7
2	0.5	35	31	43	6.5
C	14	11	11	8	39.5
J	26	13	13	9.5	36
X	41	12	10	5.5	40.5
ES	53	13	13	10.5	35
F	53	13	12	5.5	41
D	59	10	9	2	43.5
33	74	12	10	4	42
MS	80	12	10	5.5	41
7S	82	12	11	7.5	39
6	90	11	14	4	41.5
G	98	12	10	5	40
A	109	12	10	1.5	43.5
B	141	14	13	2	43

TABLE III

CREEP RUPTURE DATA OF MAR-M247 SINGLE CRYSTALS

TESTED AT 774°C and 724 MPa

SPECIMEN	ϵ_o, $\times 10^{-3}$	t_i, min	$\dot{\epsilon}_p$, $\times 10^{-1}$ hr^{-1}	ϵ_p, percent	ϵ_s, percent	$\dot{\epsilon}_m$, $\times 10^{-4}$ hr^{-1}	LIFE, hr	ORIENTATION, DEGREES FROM: [001]	[001]
2	5.4	14	8.50	34.7	-	-	0.5	43	6.5
C	9.1	13	1.68	5.91	9.20	15.18	14	8	39.5
J	2.4	19	1.64	5.48	6.95	11.49	26	9.5	36
ES	7.8	25	1.60	5.37	8.67	7.74	53	10.5	35
F	8.9	24	1.70	4.61	7.08	5.79	53	5.5	41
D	8.1	13	1.34	2.59	5.19	6.29	59	2	43.5
33	9.6	17	1.02	2.61	5.81	5.19	74	4	42
MS	4.9	24	0.87	3.71	6.55	4.95	80	5.5	41
O	6.7	26	0.24	2.04	4.19	3.02	-*	0	45
G	7.3	23	0.95	2.67	3.97	3.61	98	5	40
B	7.6	28	0.73	2.20	4.97	2.03	141	2	43

*furnace malfunctioned.

ϵ_o - instantaneous strain on loading.

t_i - incubation time.

$\dot{\epsilon}_p$, ϵ_p - primary creep rate and strain, respectively.

ϵ_s - strain at onset of steady-state creep.

$\dot{\epsilon}_m$ - minimum creep rate.

FIGURES

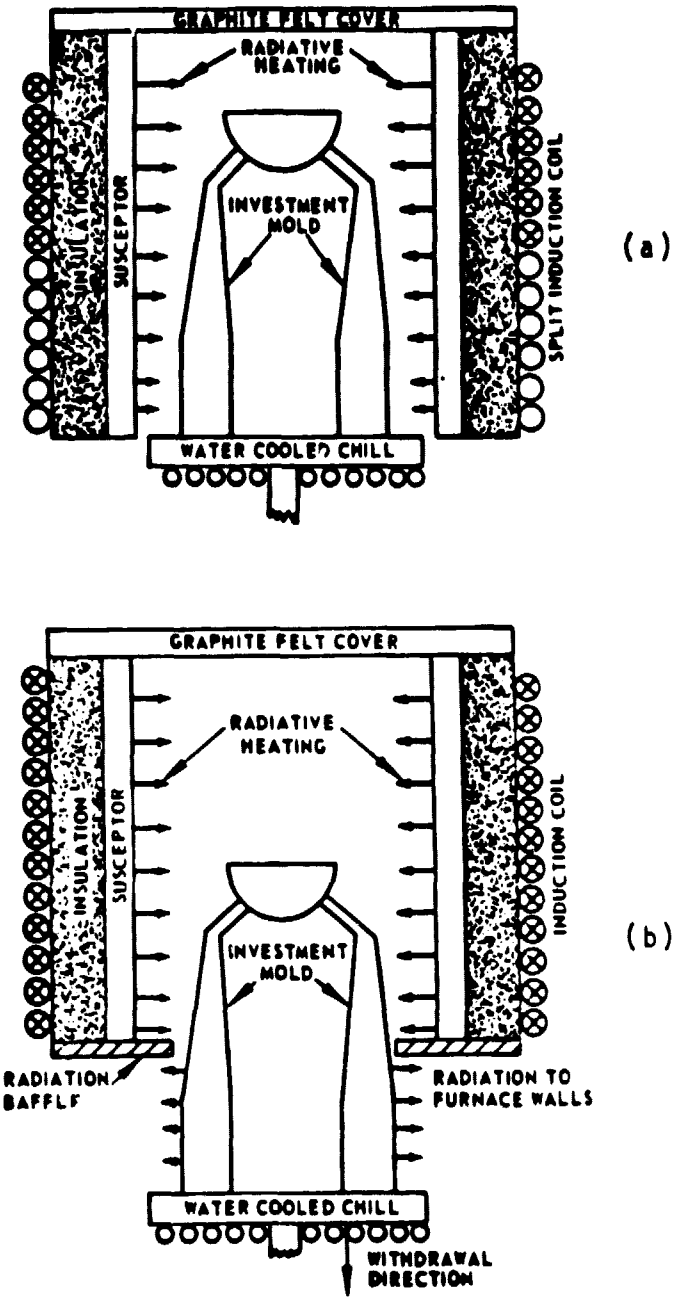

Figure 1. Schematic representation of the techniques used in the unidirectional solidification of superalloys: (a) Power Down process; and (b) High Rate Solidification, or withdrawal, process (13). X indicates power on to induction coil.

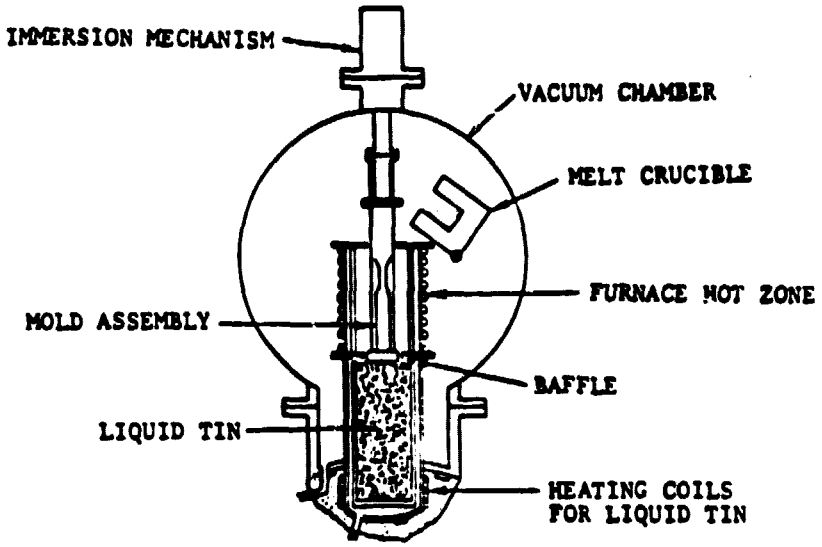

Figure 2. Schematic representation of the apparatus used to make castings by the Liquid Metal Cooling process (13).

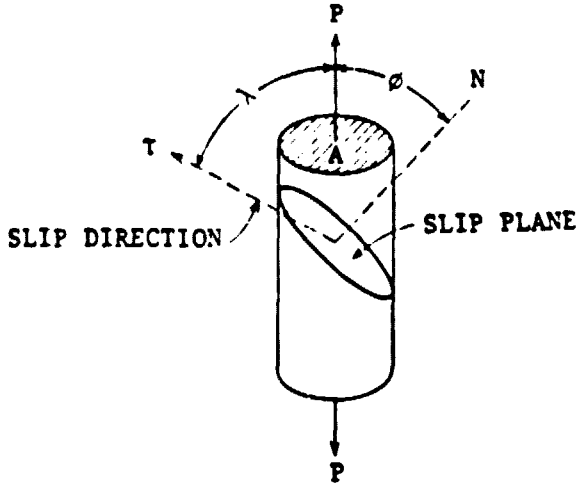

Figure 3. Schematic diagram for description of the angles, λ and ϕ, used in Schmid's Law for determining the critical resolved shear stress (25).

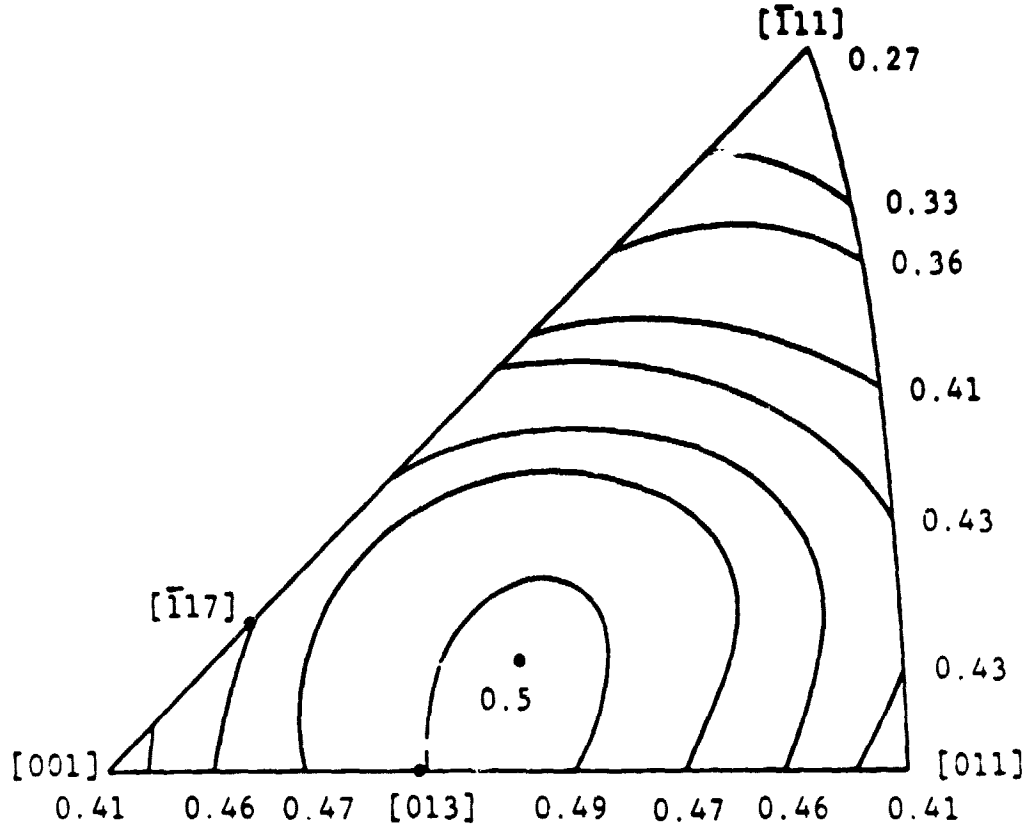

Figure 4. Schmid factor contours for the (111)[$\bar{1}$01] slip system which have been superimposed on the standard [001] - [011] - [$\bar{1}$11] stereographic triangle.

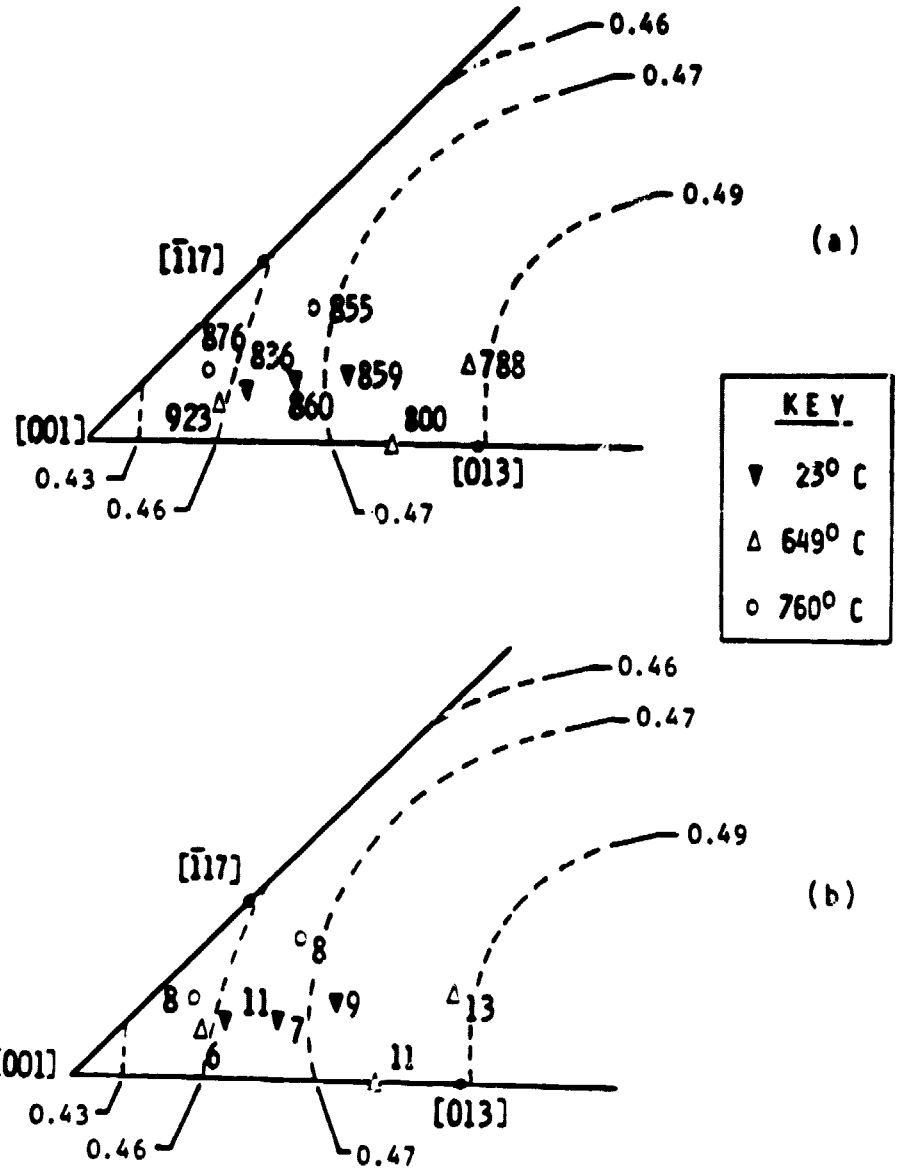

Figure 5. Portions of stereographic triangle showing the tensile behavior as a function of orientation for Mar-M247 single crystals tested at 23, 649, and 760°C (24). The numbers associated with the orientations indicate: (a) yield strength, MPa; and (b) elongation, percent.

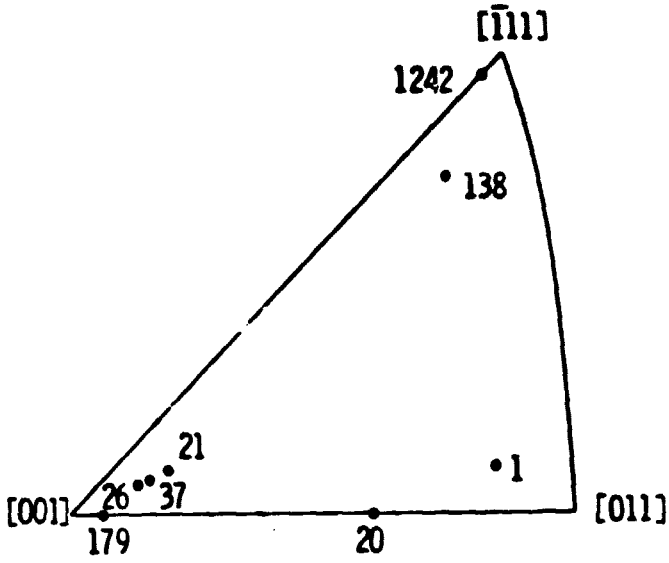

(a) 774°C, 724 MPa

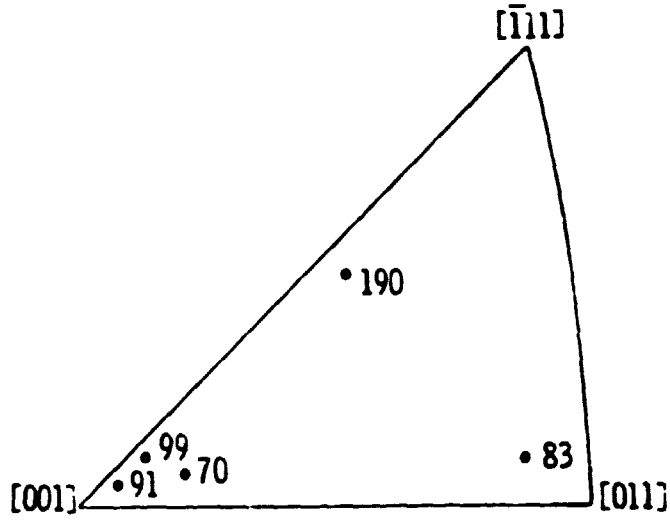

(b) 982°C, 207 MPa

Figure 6. Stress rupture lives shown as a function of orientation for exothermically cast Mar-M247 single crystals tested under two different conditions (24). The numbers associated with the orientations indicate the lives in hours.

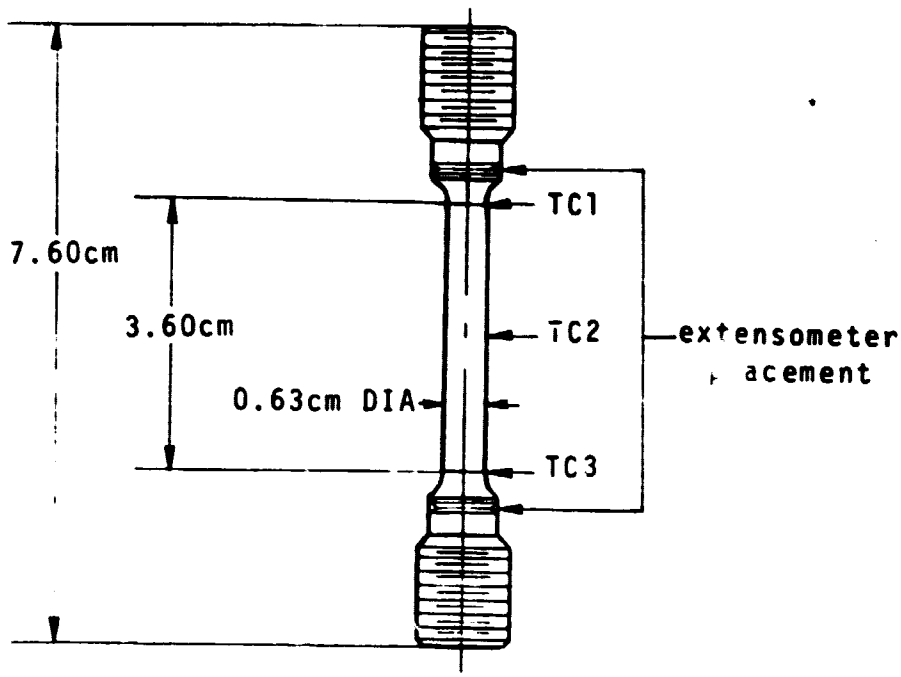

Figure 7. Specimen configuration which shows the location of the ridges in which the extensometer knife edges were placed. Location of thermocouples (TC1, TC2, TC3) is also shown.

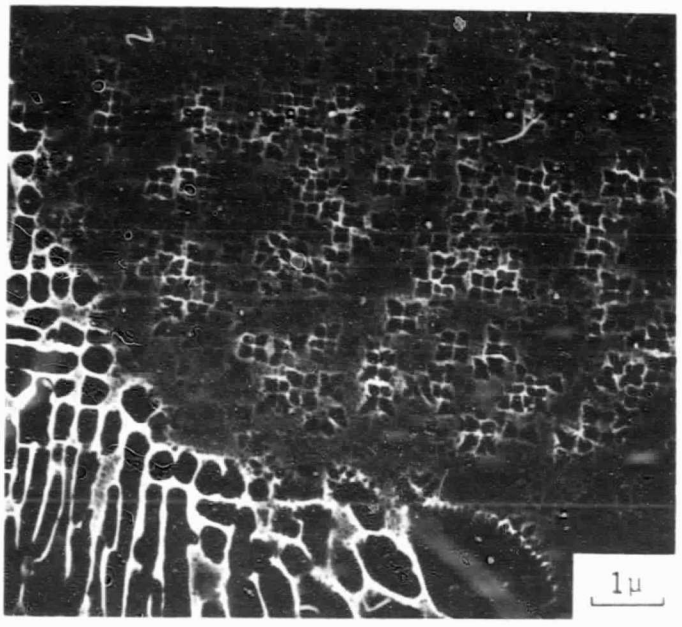

Figure 8. Scanning electron micrograph showing the γ - γ' eutectic (lower left corner) contained in the interdendritic region of a fully heat treated Mar-M247 single crystal.

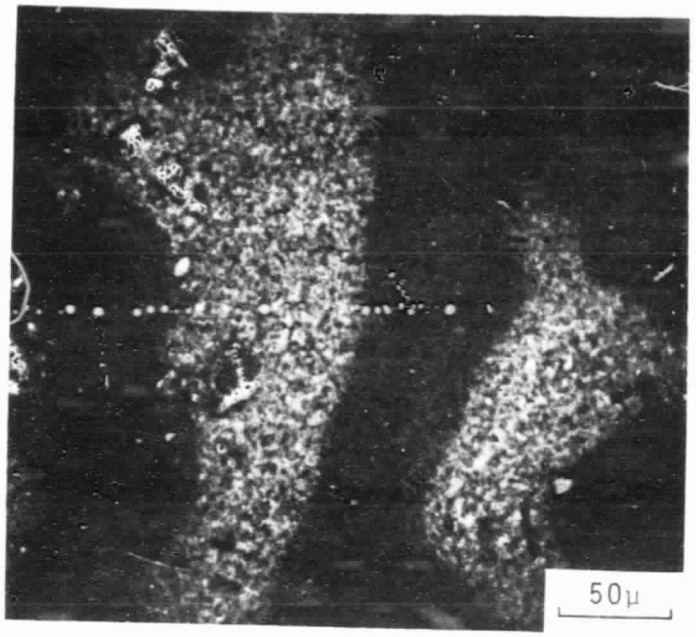

(a)

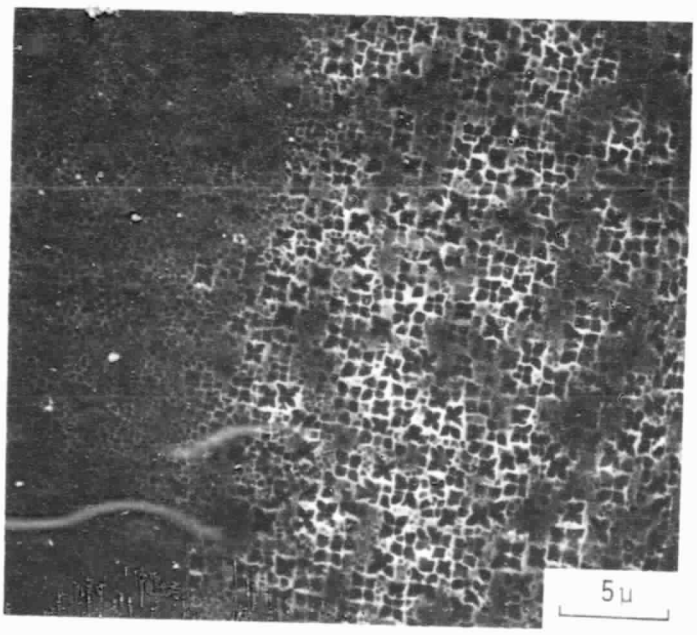

(b)

Figure 9. Scanning electron micrographs of a fully heat treated Mar-M247 single crystal showing the (a) coring produced during solidification, and (b) change in γ' size at the interface between a dendrite core and interdendritic region.

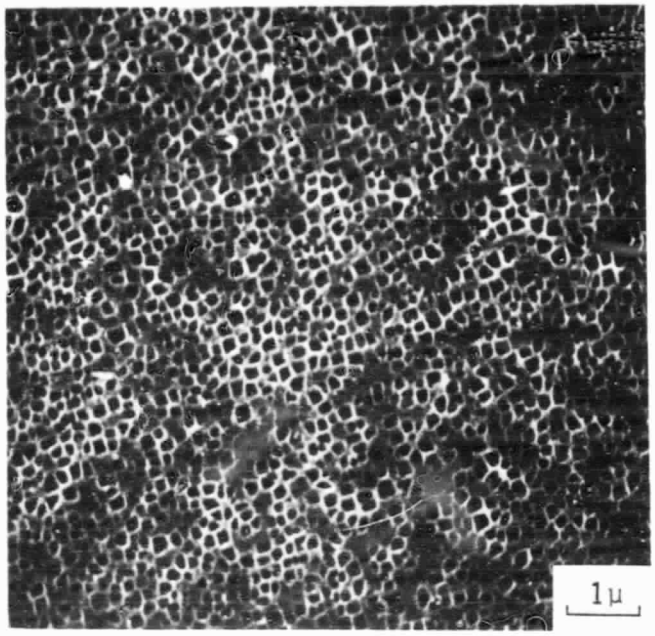

(a)

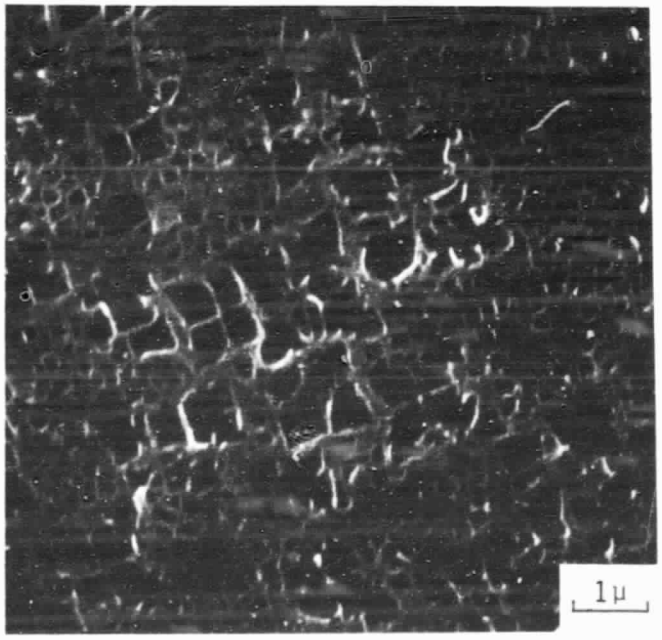

(b)

Figure 10. Scanning electron micrographs showing the γ' particles within the (a) dendrite centers and (b) interdendritic regions of a fully heat treated Mar-M247 single crystal.

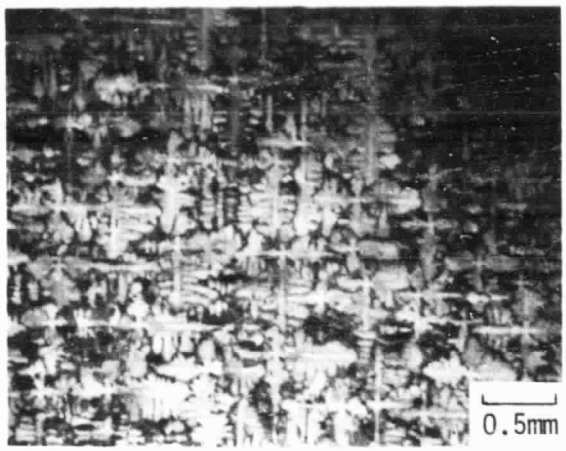

(a) cross section

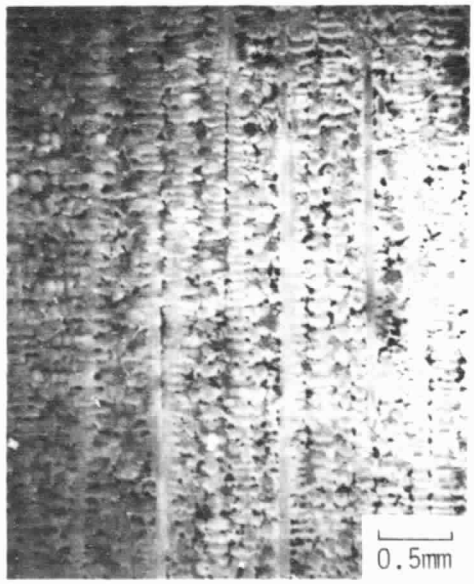

(b) longitudinal section

Figure 11. Macrostructure of a cube-oriented Mar-M247 single crystal.

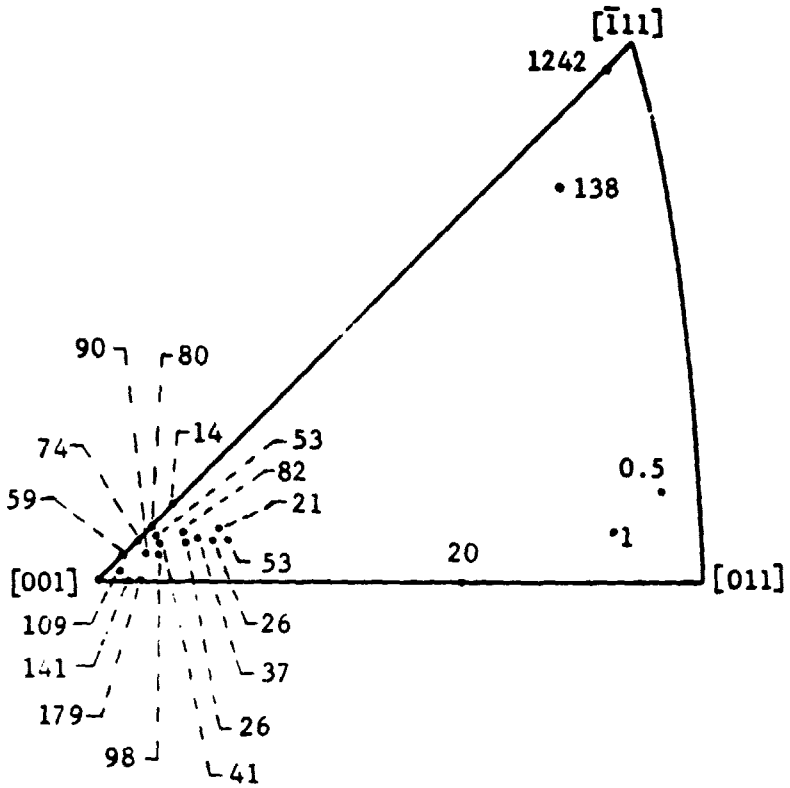

Figure 12. Stress rupture lives shown as a function of orientation for Mar-M247 single crystals tested at 774°C and 724 MPa. The numbers associated with the orientations are the lives in hours.

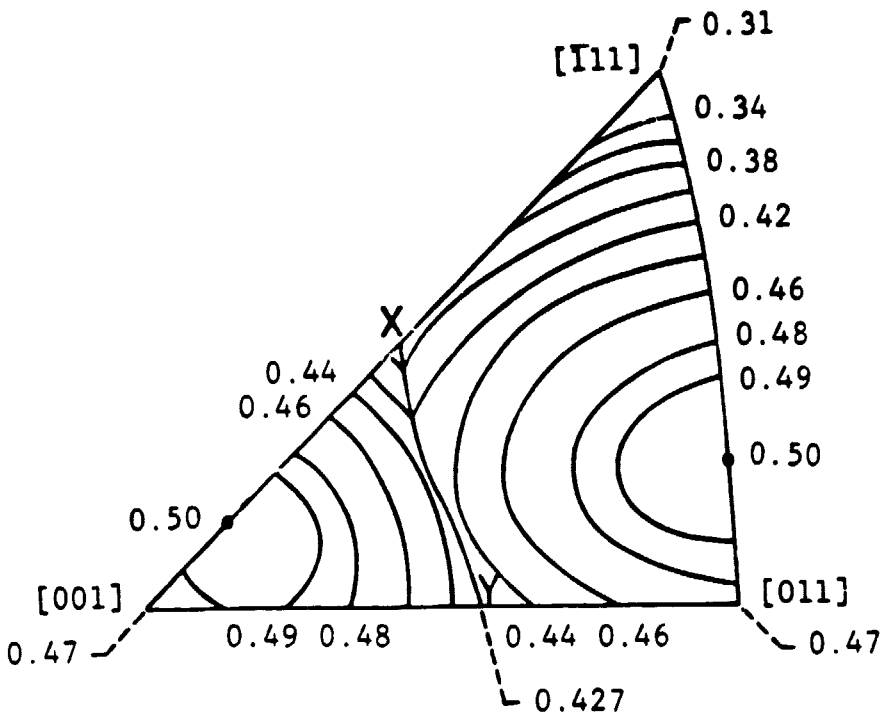

Figure 13. Schmid factor contours for the most highly stressed {111}<112> slip systems. X - Y is the dividing line between the two {111}<112> slip systems which have the highest Schmid factors. The $(\bar{1}11)[i\bar{1}2]$ slip system is operative for orientations to the left of the X - Y line; the $(111)[\bar{2}11]$ slip system is operative to the right of the X - Y line.

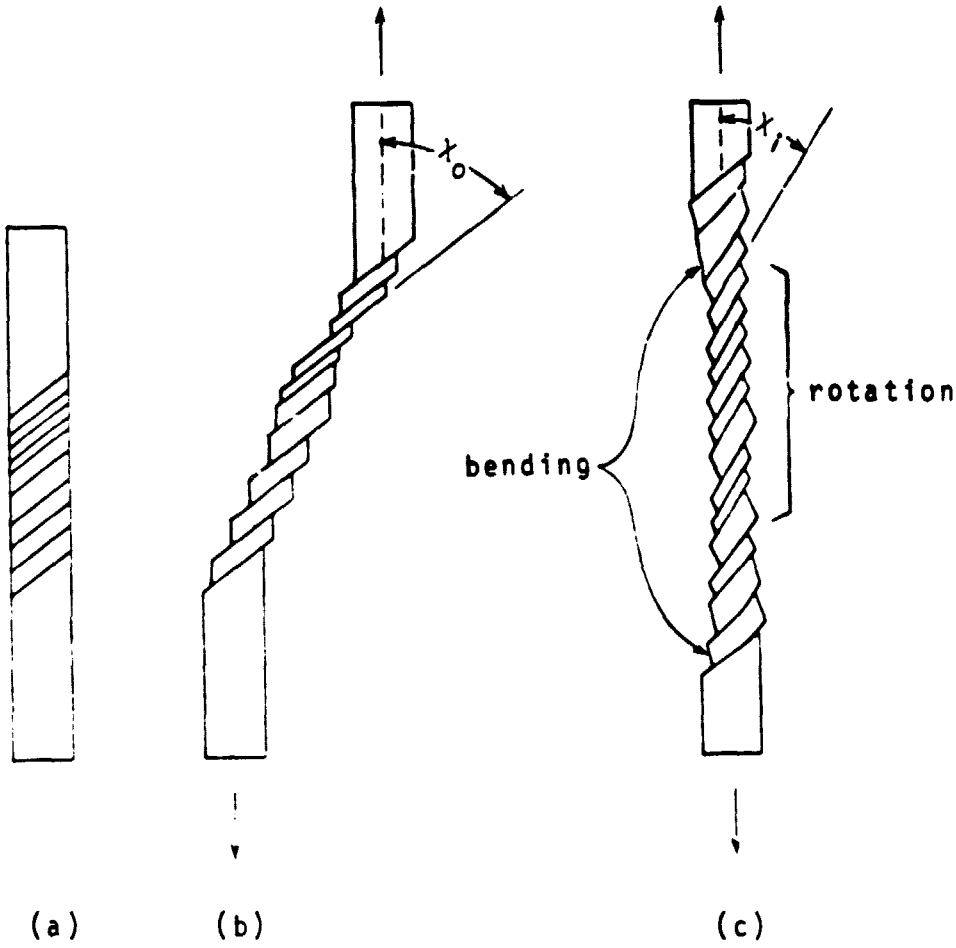

Figure 14. Schematic diagram showing the orientation of the slip planes in a single crystal bar. (a) Prior to deformation; (b) after deformation without grip constraint, where crystal segments move relative to one another but with no slip plane rotation; and (c) after deformation with grip constraint, revealing slip plane rotation in gage section (note $\chi_i < \chi_o$) (41).

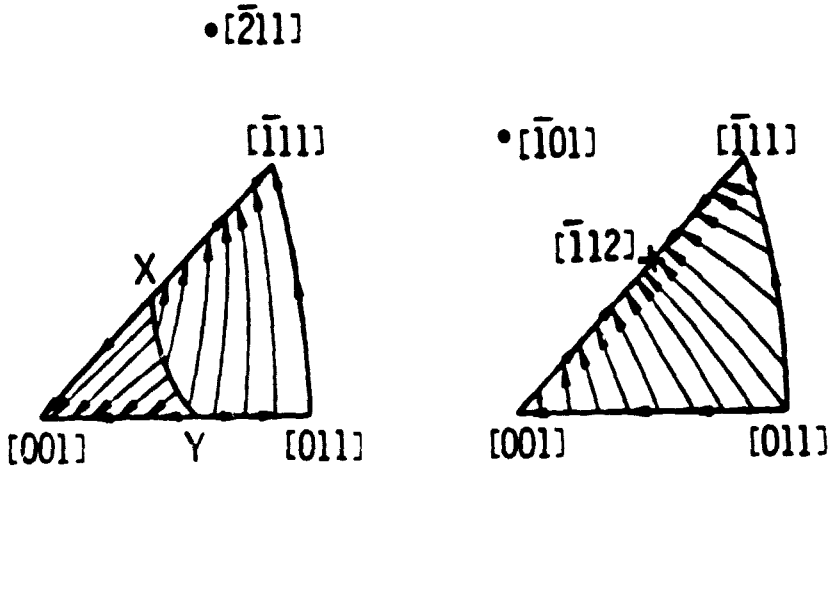

(a) {111}<112> slip (b) (111) [1̄01] slip

Figure 15. Directions of rotation in standard stereographic triangle for single crystals under two different slip systems.

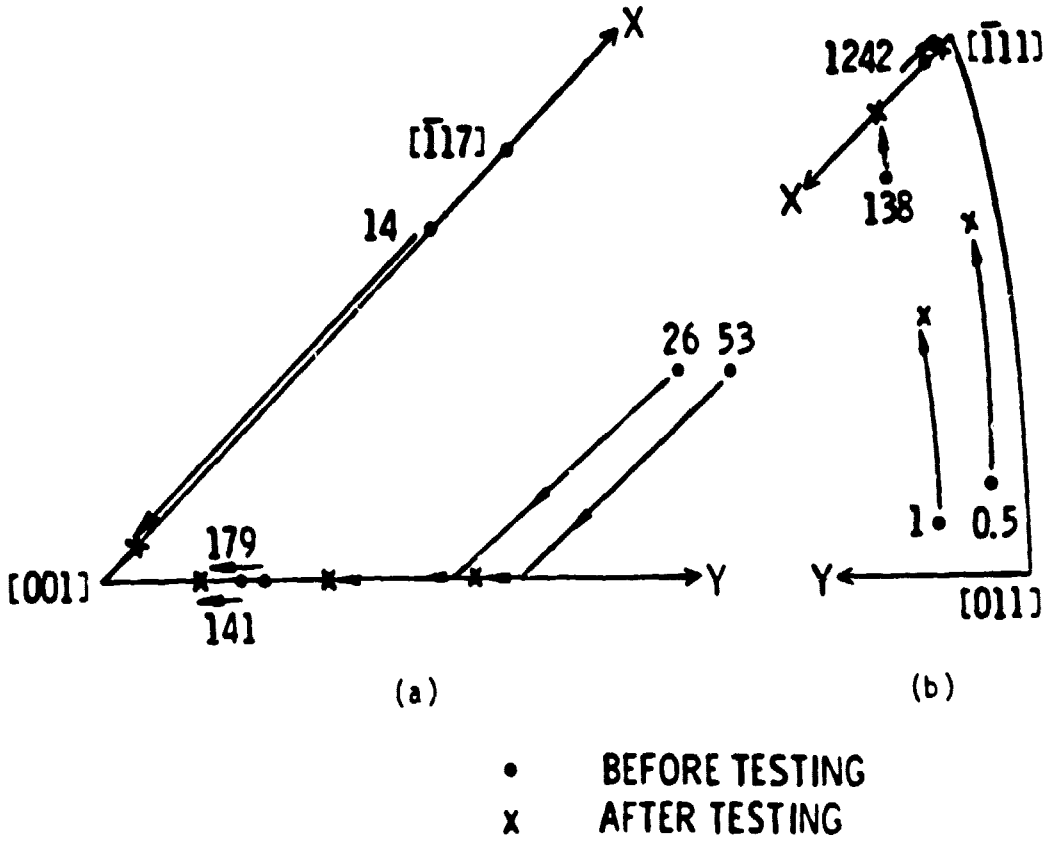

Figure 16. Lattice rotations for selected Mar-M247 single crystals which were stress rupture tested at 774°C and 724 MPa: (a) [001] corner; and (b) [$\bar{1}$11] - [011] portion of stereographic triangle. The arrows depict the directions of rotation for the crystals. The numbers associated with the rotations represent the lives in hours.

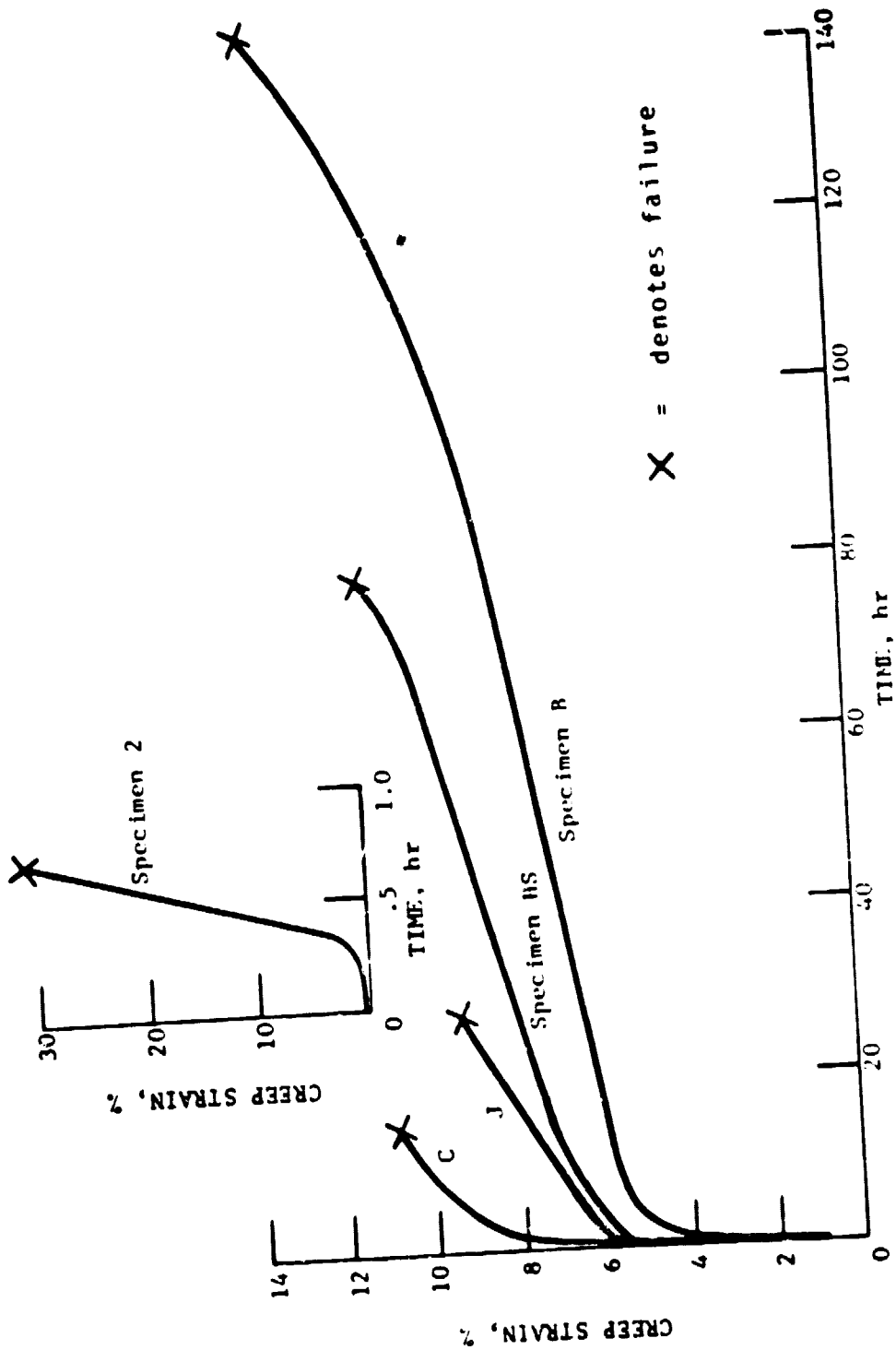

Figure 17. Creep curves of selected Mar-M247 specimens tested at 774°C and 724 MPa.

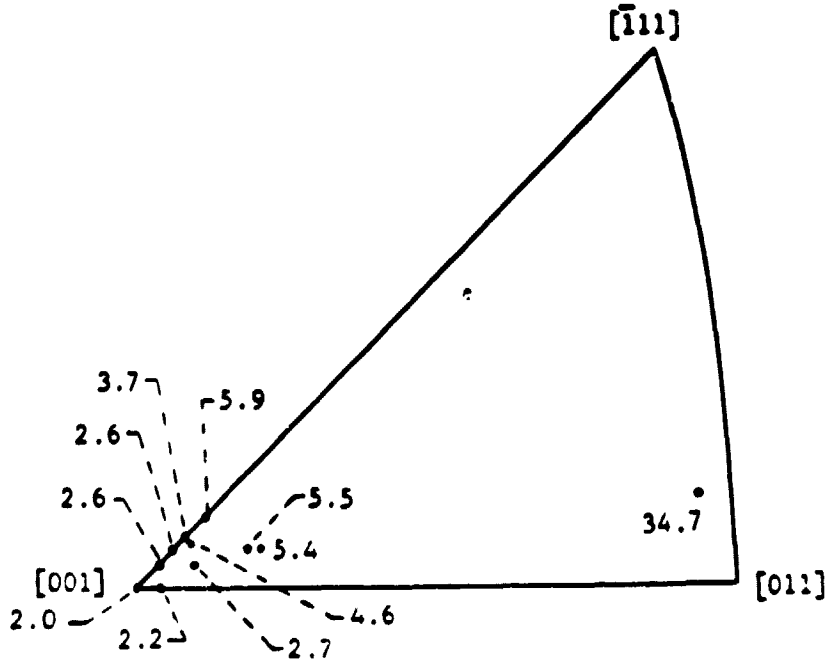

(a) Primary creep strain, ε_p (%)

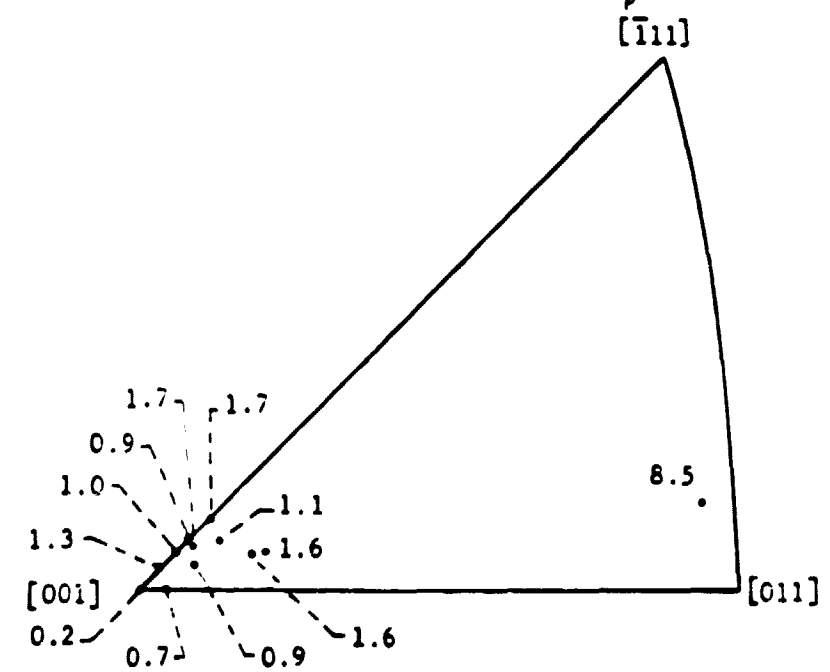

(b) Primary creep rate, $\dot{\varepsilon}_p$ (x 10^{-1} hr^{-1})

Figure 18. Creep rupture data shown as a function of orientation for Mar-M247 single crystals tested at 774°C and 724 MPa.

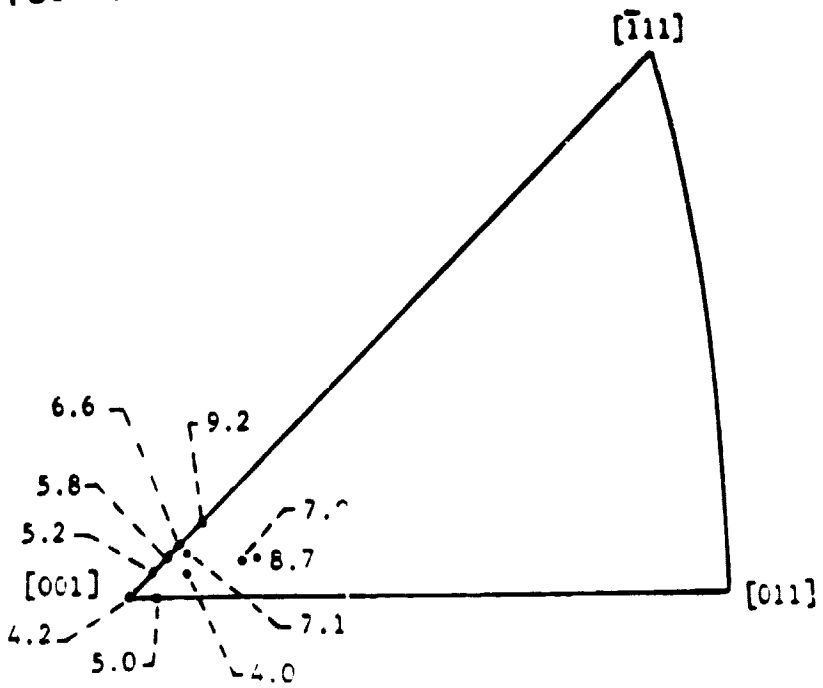

(c) Strain at onset of second-stage creep, ε_s (%)

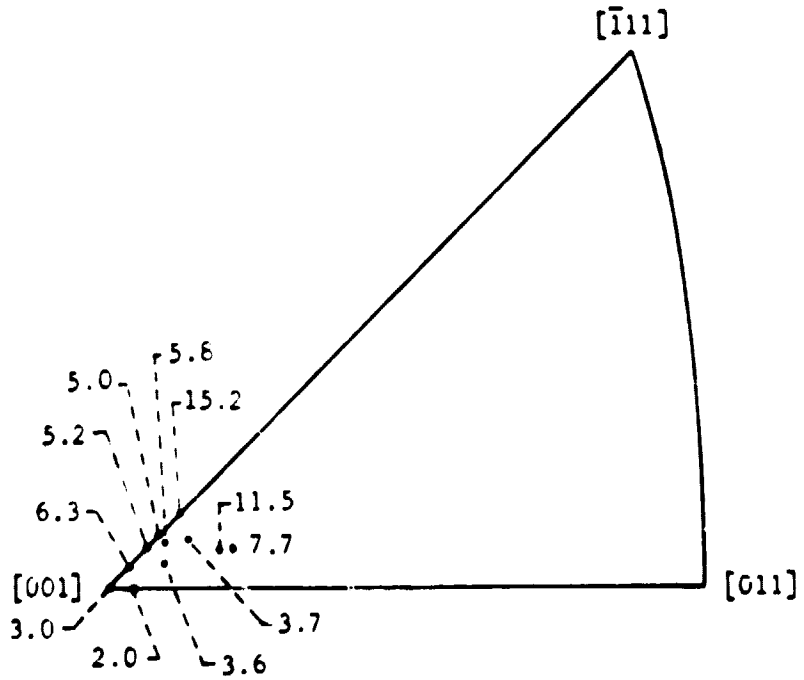

(d) Minimum creep rate, $\dot{\varepsilon}_m$ (x 10^{-4} hr^{-1})

Figure 18 concluded

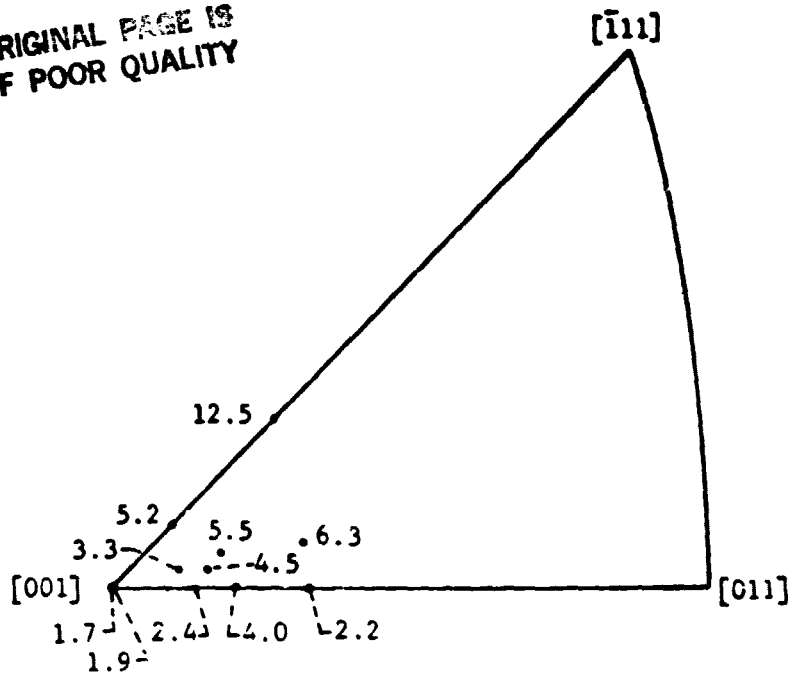

(a) Primary creep strain (%)

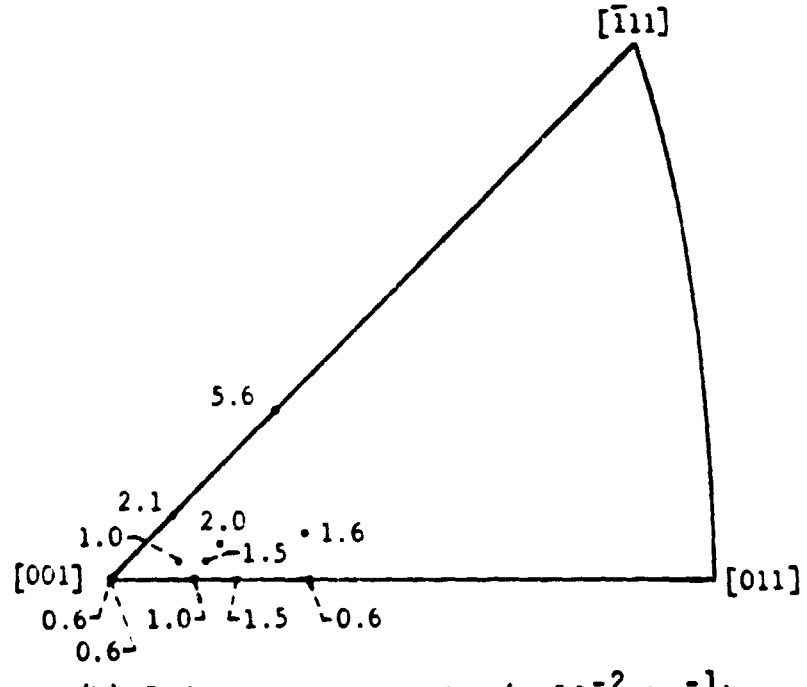

(b) Primary creep rate (x 10^{-2} hr^{-1})

Figure 19. Mar-M200 creep data shown as a function of orientation for single crystals tested at 760°C and 689 MPa (26).

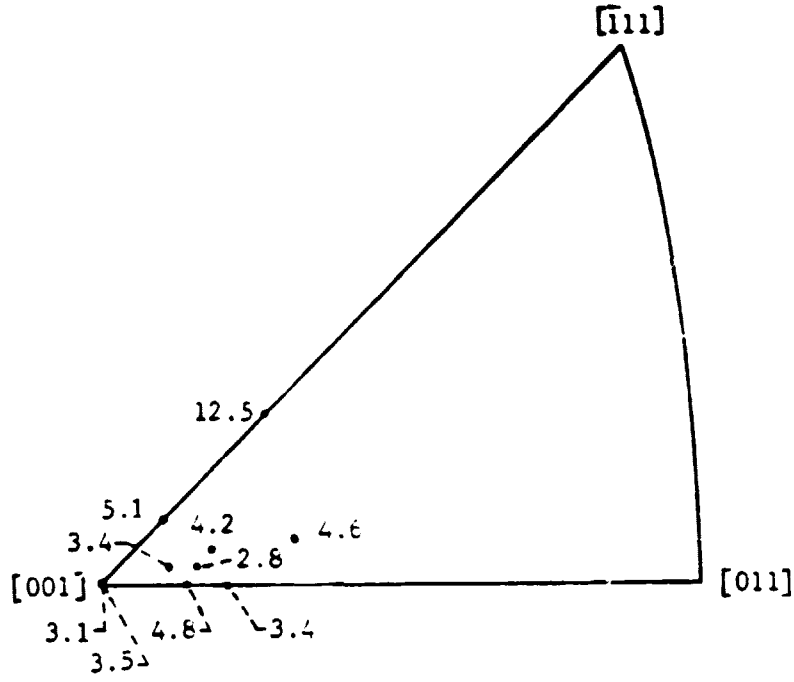

(c) Steady-state creep rate (x 10^{-4} hr^{-1})

Figure 19 concluded

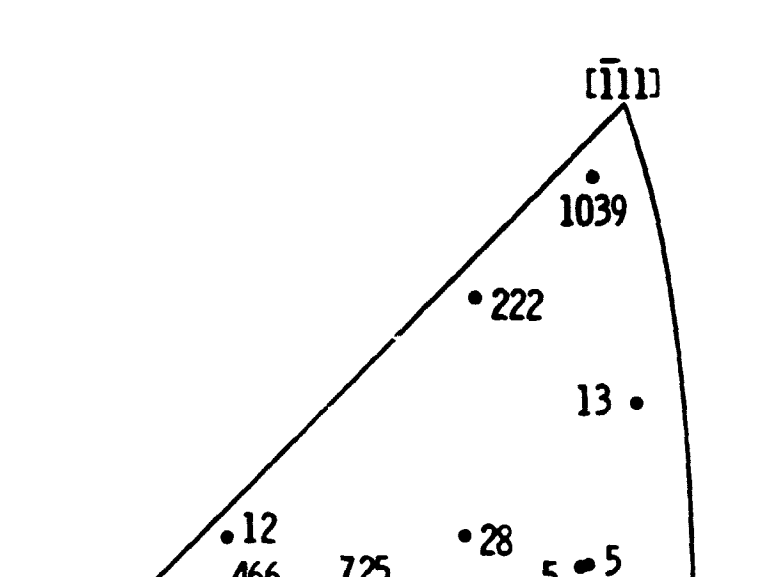

Figure 20. Stress rupture lives shown as a function of orientation for Mar-M200 single crystals tested at 760°C and 689 MPa (10). The numbers associated with the orientations are the lives in hours.

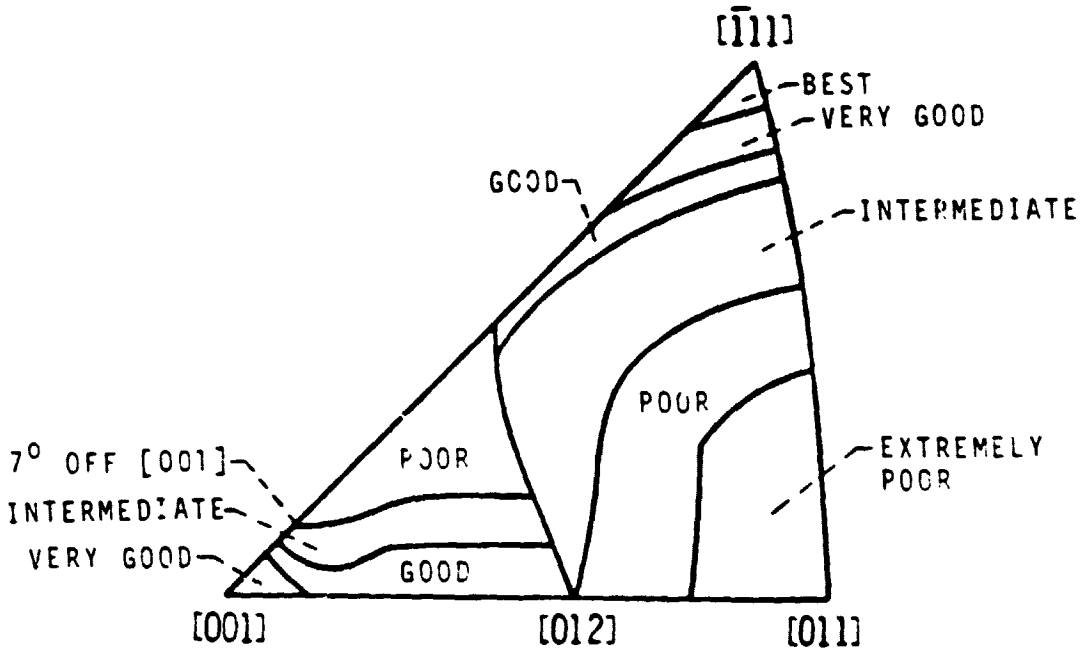

Figure 21. Suggested regimes of stress rupture lives for Mar-M247 and Mar-M200 single crystals at about 760°C.

APPENDICES

APPENDIX A

CALCULATION FOR SINGLE GLIDE IN TENSION

The amount of elongation, ϵ, necessary for a crystal gliding in single slip to rotate into a duplex slip orientation was calculated from an equation for single glide in tension (43,44):

$$\epsilon = \frac{\sin \lambda_o}{\sin \lambda} - 1 \qquad \text{(Eq. A)}$$

where λ_o is the angle between the slip direction and the initial single slip orientation and λ is the angle between the slip direction and the duplex slip boundary orientation. The $[1\bar{1}2]$ is the slip direction during first-stage creep for the Mar-M247 and Mar-M200 single crystals considered below.

Mar-M247 Single Crystal

The elongation necessary for the Mar-M247 Crystal C to reach the duplex slip [001] - X boundary was computed as follows:

$$\epsilon = \frac{\sin 43}{\sin 35} - 1$$

$$\epsilon = 18.9\ \%$$

where 43° is the angle between the $[1\bar{1}2]$ and the initial orientation of the crystal; and 35° is the angle between the $[1\bar{1}2]$ and the duplex slip boundary orientation. Thus, the elongation necessary for this crystal to obtain intersecting slip regions of the stereographic triangle was 18.9%. However, the elongation measured after specimen failure was only 11%. This computation provides further verification that Specimen C never reached the multiple slip [001] orientation.

Mar-M200 Single Crystal

The elongation of a 12-hour life Mar-M200 (10) single crystal is considered next in some detail. The initial orientation of this specimen is represented by the solid dot in Figure A, and the duplex slip orientation, toward which this crystal is rotating, is represented by the open circle along the [001] - [011] boundary.

The elongation necessary for this crystal to reach the duplex slip boundary was computed as follows:

$$\varepsilon = \frac{\sin 47.5}{\sin 36} - 1$$

$$\varepsilon = 25.4\ \%$$

Thus, the elongation necessary for this crystal to obtain intersecting slip regions of the stereographic triangle was 25.4%, approximately 2.5 times larger than the 10.3% elongation (10) measured after specimen failure. It appears according to this computation that this specimen never reached the duplex slip boundary.

To calculate the position of the final orientation of this Mar-M200 specimen after creep rupture testing, the measured elongation after failure was utilized by rearranging Eq. A as follows:

$$\sin \lambda = \frac{\sin \lambda_o}{1 + \varepsilon}$$

$$\sin \lambda = \frac{\sin 47.5}{1 + 0.103}$$

$$\sin \lambda = 0.668$$

$$\lambda = 41.9^\circ$$

where 41.9° is the angle between the $[1\bar{1}2]$ and the calculated final orientation of the crystal. This angle corresponds to a final orientation which is 6° from the duplex slip [0?1] - [011] boundary. This calculated final orientation is represented by the x in Figure A and shows that this specimen was not able to benefit from the strengthening effects of intersecting slip. An extremely

short creep rupture life of 12 hours resulted for this crystal.

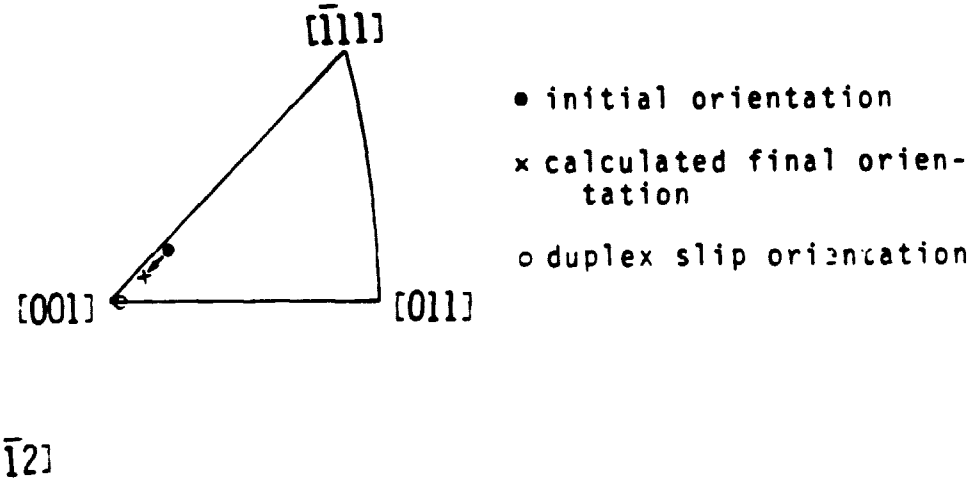

Figure A. Stereographic triangle showing the calculated rotation of a Mar-M200 single crystal (10) tested at 760°C and 689 MPa. Rupture life of this specimen was 12 hours.

APPENDIX B

METHODS FOR MEASURING CREEP RUPTURE DATA

The metnods utilizeo for measuring the creep rupture data of the Mar-M247 single crystals which were tested at 774^{o}C and 724 MPa are described below. The definitions of ε_o and t_i are illustrated in the upper left corner of Figure B, where the initial portion of the typical creep curve of Specimen G has been expanded to show the appropriate detail for short-time creep. The instantaneous strain, ε_o, is the elastic strain which occurs upon initial loading of the specimen. The incubation time, t_i, is defined as the amount of time after loading up to the point where measurable creep strain is detecteu. This was taken to be the point of tangency at which the linear primary creep region begins.

The remaining creep rates and strains obtained are illustrated in the full creep curve of Figure B. Tne primary creep rate, $\dot{\varepsilon}_p$, is the slope of the linear portion of tne primary creep region. The primary creep strain, ε_p, is defined as the total amount of strain from ε_o to the point of tangency where the primary creep region starts to deviate from linearity. The strain at the onset of second-stage creep, ε_s, corresponds to the amount of strain from ε_o to the point of

tangency at which the linear portion of the steady-state creep regime begins. The minimum creep rate, $\dot{\epsilon}_m$, is the minimum slope at the onset of the steady-state creep regime.

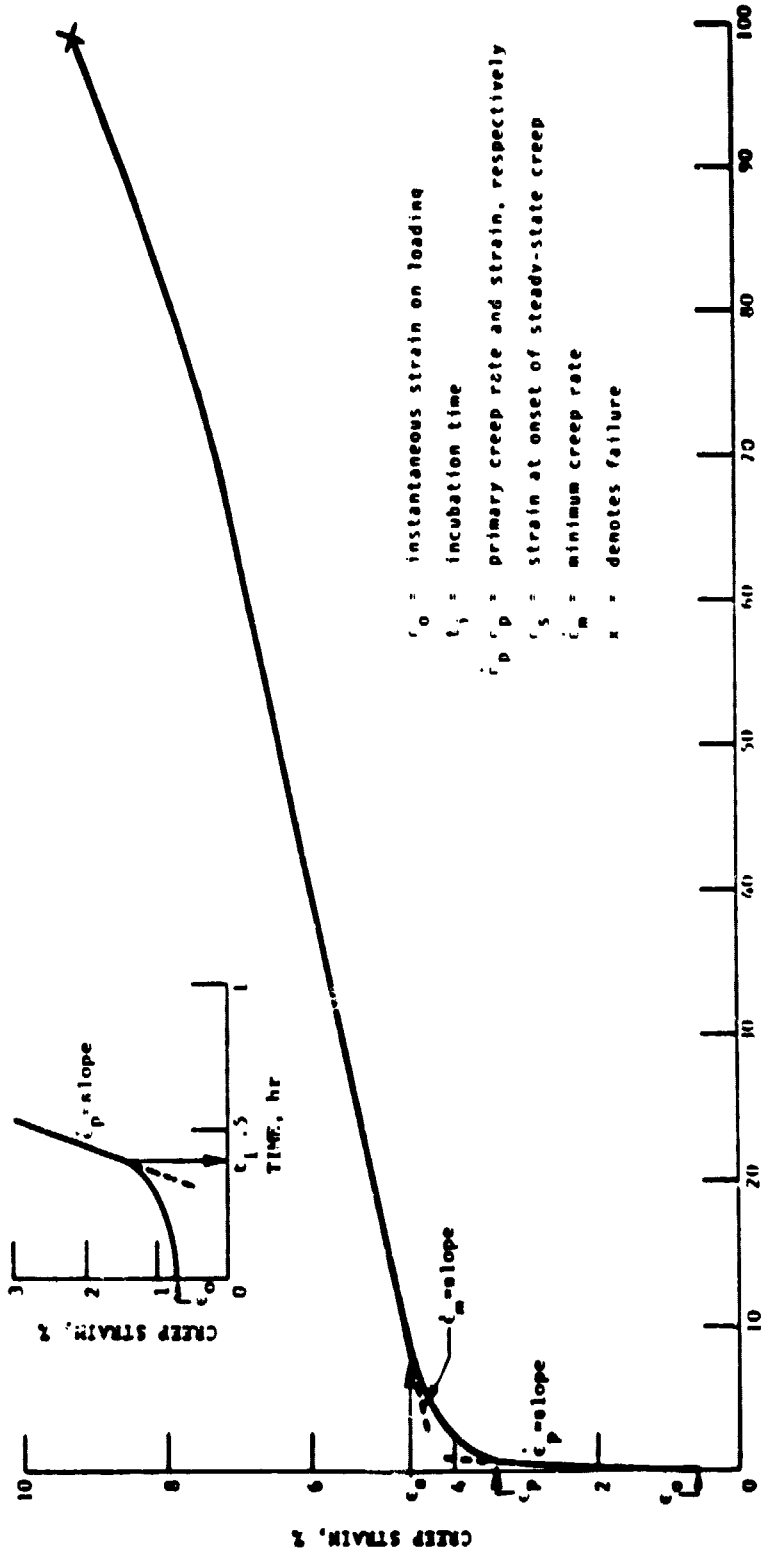

Figure B. A typical creep curve (Specimen G) for the Mar-M247 single crystals tested at 774C and 724 MPa illustrating the definitions of the creep rupture data obtained. Short-time creep is expanded in the upper left corner.

APPENDIX C

COMPUTATION OF EFFECTIVE STRESS LEVEL AT ONSET OF STEADY-STATE CREEP

The effective stress level, σ_e, at the onset of steady-state creep was determined as follows:

$$\sigma_e = \frac{P}{A} \qquad \text{(Eq. C - 1)}$$

where P is the load and A is the cross-sectional area at the onset of steady-state creep. Assuming constancy of volume,

$$A_o L_o = AL \qquad \text{(Eq. C - 2)}$$

where A_o is the original cross-sectional area, L_o is the original gage length, and L is the gage length at the onset of steady-state creep. The strain, e, of the specimen at the onset of second-stage creep is given by:

$$e = \frac{L}{L_o} - 1 \qquad \text{(Eq. C - 3)}$$

Rearranging and combining,

$$\sigma_e = \frac{P}{A_o} (e + 1) \qquad \text{(Eq. C - 4)}$$

where P/A_o is the nominal stress level.

The nominal stress level for the Mar-M247 single crystals tested at 774^{o}C was 724 MPa. The strain at the onset of steady-state creep, ε_s, is listed in Table III for all the Mar-M247 single crystals creep rupture tested. This strain, ε_s, was substituted into e in Eq. C-4. Thus, Specimen B, which had a strain at the onset of steady-state creep equal to 4.97%, was computed to have an effective stress level of 760 MPa at the onset of steady-state creep. Specimen C had a strain of 9.20% at the beginning of steady-state creep and was computed to have a significantly higher effective stress level of 790 MPa at the onset of steady-state creep.

END DATE
JAN 31, 1983